

JWST NIRSpec High-resolution Spectroscopy of MACS0647–JD at $z = 10.167$: Resolved [OII] Doublet and Electron Density in an Early Galaxy

ABDURRO'UF ^{1,2} REBECCA L. LARSON ³ DAN COE ^{2,4,1} TIGER YU-YANG HSIAO ^{1,2}
JAVIER ÁLVAREZ-MÁRQUEZ ⁵ ALEJANDRO CRESPO GÓMEZ ⁵ ANGELA ADAMO ⁶ RACHANA BHATAWDEKAR ⁷
ARJAN BIK ⁶ LARRY D. BRADLEY ² CHRISTOPHER J. CONSELICE ⁸ PRATIKA DAYAL ⁹ JOSE M. DIEGO ¹⁰
SEIJI FUJIMOTO ^{11,*} LUKAS J. FURTAK ¹² TAYLOR A. HUTCHISON ^{13,†} INTAE JUNG ¹⁴ MEGHANA KILLI ¹⁵
VASILY KOKOREV ¹⁶ MATILDE MINGOZZI ² COLIN NORMAN ^{1,2} TOM RESSEQUIER ^{1,2} MASSIMO RICOTTI ¹⁷
JANE R. RIGBY ¹³ EROS VANZELLA ¹⁸ BRIAN WELCH ^{13,17} ROGIER A. WINDHORST ¹⁹ XINFENG XU ²⁰ AND
ADI ZITRIN ¹²

¹*Department of Physics and Astronomy, The Johns Hopkins University, 3400 N Charles St. Baltimore, MD 21218, USA*

²*Space Telescope Science Institute (STScI), 3700 San Martin Drive, Baltimore, MD 21218, USA*

³*School of Physics and Astronomy, Rochester Institute of Technology, 84 Lomb Memorial Drive, Rochester, NY 14623, USA*

⁴*Association of Universities for Research in Astronomy (AURA), Inc. for the European Space Agency (ESA)*

⁵*Centro de Astrobiología (CAB), CSIC-INTA, Ctra. de Ajalvir km 4, Torrejón de Ardoz, E-28850, Madrid, Spain*

⁶*Department of Astronomy, Stockholm University, Oscar Klein Centre, AlbaNova University Centre, 106 91 Stockholm, Sweden*

⁷*European Space Agency (ESA), European Space Astronomy Centre (ESAC), Camino Bajo del Castillo s/n, 28692 Villanueva de la Cañada, Madrid, Spain*

⁸*Jodrell Bank Centre for Astrophysics, University of Manchester, Oxford Road, Manchester UK*

⁹*Kapteyn Astronomical Institute, University of Groningen, 9700 AV Groningen, The Netherlands*

¹⁰*Instituto de Física de Cantabria (CSIC-UC). Avda. Los Castros s/n. 39005 Santander, Spain*

¹¹*The University of Texas at Austin, Department of Astronomy, Austin, TX, United States*

¹²*Physics Department, Ben-Gurion University of the Negev, P.O. Box 653, Be'er-Sheva 84105, Israel*

¹³*Observational Cosmology Lab, NASA Goddard Space Flight Center, Greenbelt, MD 20771, USA*

¹⁴*Space Telescope Science Institute, 3700 San Martin Drive Baltimore, MD 21218, United States*

¹⁵*Instituto de Estudios Astrofísicos, Facultad de Ingeniería y Ciencias, Universidad Diego Portales, Av. Ejército 441, Santiago 8370191, Chile*

¹⁶*Kapteyn Astronomical Institute, University of Groningen, P.O. Box 800, 9700 AV Groningen, The Netherlands*

¹⁷*Department of Astronomy, University of Maryland, College Park, 20742, USA*

¹⁸*INAF – OAS, Osservatorio di Astrofisica e Scienza dello Spazio di Bologna, via Gobetti 93/3, I-40129 Bologna, Italy*

¹⁹*School of Earth and Space Exploration, Arizona State University, Tempe, AZ 85287-1404, USA*

²⁰*Department of Physics and Astronomy, Northwestern University, 2145 Sheridan Road, Evanston, IL, 60208, USA*

Submitted to ApJ

ABSTRACT

We present JWST/NIRSpec high-resolution spectroscopy G395H/F290LP of MACS0647–JD, a gravitationally lensed galaxy merger at $z = 10.167$. The new spectroscopy, which is acquired for the two lensed images (JD1 and JD2), detects and resolves emission lines in the rest-frame ultraviolet (UV) and blue optical, including the resolved [O II] $\lambda\lambda 3726, 3729$ doublet, [Ne III] $\lambda 3870$, He I $\lambda 3890$, H δ , H γ , and [O III] $\lambda 4363$. This is the first observation of the resolved [O II] $\lambda\lambda 3726, 3729$ doublet for a galaxy at $z > 8$. We measure a line flux ratio [O II] $\lambda 3729/\lambda 3726 = 0.9 \pm 0.3$, which corresponds to an estimated electron density of $\log(n_e/\text{cm}^{-3}) = 2.9 \pm 0.5$. This is significantly higher than the electron densities of local galaxies reported in the literature. We compile the measurements from the literature and further analyze the redshift evolution of n_e . We find that the redshift evolution follows the power-law form of $n_e = A \times (1 + z)^p$ with $A = 54^{+31}_{-23} \text{ cm}^{-3}$ and $p = 1.2^{+0.4}_{-0.4}$. This power-law

Corresponding author: Abdurro'uf

fabdurr1@jhu.edu

form may be explained by a combination of metallicity and morphological evolution of galaxies, which become, on average, more metal-poor and more compact with increasing redshift.

Keywords: Galaxies (573), High-redshift galaxies (734), Early universe (435), Strong gravitational lensing (1643), Galaxy spectroscopy (2171)

1. INTRODUCTION

Understanding the physical conditions in star-forming galaxies, including the interstellar medium (ISM), is essential for a complete picture of the evolution of the stellar and gaseous content of galaxies. Spectroscopy of galaxies in the rest-frame ultraviolet (UV) and optical provides a wealth of emission line diagnostics for characterizing the ISM in galaxies (e.g., see review by Kewley et al. 2019b). The relative strengths of the emission lines are mainly driven by the ISM properties, including the chemical abundance, shape of the ionizing radiation field, ionization state, gas density, and temperature (e.g., Kewley & Dopita 2002; Dopita et al. 2006a,b).

Before the launch of the JWST, the observations of rest-frame UV and optical spectra of high-redshift ($z \gtrsim 3$) galaxies were very challenging because of the lack of highly sensitive (i.e., deep) near-infrared (NIR) spectroscopy. Only a few spectroscopic surveys have been conducted to observe rest-frame UV and optical spectroscopy of high- z galaxies out to $z \sim 4$ using 8–10 m class telescopes (e.g., Kriek et al. 2015; Le Fèvre et al. 2015; Bacon et al. 2017; Pentericci et al. 2018; Urrutia et al. 2019).

Since the launch of JWST (Rigby et al. 2023; Gardner et al. 2023), with its NIR and mid-infrared (MIR) spectroscopic capabilities, the rest-frame UV and optical emission lines of $z > 2$ galaxies have become easily accessible, enabling the study of the ISM properties in galaxies at high redshift (toward the reionization era). Several studies use JWST/Near Infrared Spectrograph (NIRSpec) spectroscopy (Jakobsen et al. 2022; Böker et al. 2023) to study the properties of ISM in galaxies up to $z \sim 9$ (e.g., Fujimoto et al. 2022; Curti et al. 2023; Fujimoto et al. 2023; Tang et al. 2023; Bunker et al. 2023; Heintz et al. 2023a,b; Reddy et al. 2023; Nakajima et al. 2023; Hsiao et al. 2023a; Isobe et al. 2023; Jung et al. 2023; Cameron et al. 2023; Sanders et al. 2024; Backhaus et al. 2024). Those studies found that high- z galaxies have significantly lower gas-phase metallicity (e.g., Fujimoto et al. 2023; Heintz et al. 2023a; Nakajima et al. 2023; Williams et al. 2023) and higher electron density

(n_e ; e.g., Reddy et al. 2023; Isobe et al. 2023) than low- z galaxies.

The electron density of the H II regions is one of the important properties of the ISM because it is an excellent tracer of the gas density in the star-forming regions. This quantity can be estimated using density-sensitive emission line ratios, including [O II] $\lambda 3729/\lambda 3726$, [S II] $\lambda 6716/\lambda 6731$, C III] $\lambda 1909/\lambda 1907$ (e.g., Kewley et al. 2019b). In star-forming regions, the excitation energy between the two lines of those doublets is proportional to the thermal electron density. Therefore, the relative excitation rates depend only on the collision strengths of the electrons (Osterbrock 1989). This makes the flux ratio between the two lines a perfect diagnostic for the electron density.

Before JWST, several large spectroscopic surveys investigated the evolution of the electron density based on [O II] $\lambda\lambda 3726, 3729$ and [S II] $\lambda\lambda 6716, 6731$ (i.e., from low-ionization regions). They found that n_e declines from $\sim 200 \text{ cm}^{-3}$ at $z \sim 3$ to $\sim 30 \text{ cm}^{-3}$ at $z \sim 0$ (e.g., Steidel et al. 2014; Sanders et al. 2016; Kaasinen et al. 2017; Kashino et al. 2017; Harshan et al. 2020; Davies et al. 2021; Berg et al. 2022). Due to the lack of highly sensitive NIR spectroscopy, there was a lack of n_e studies at $z \gtrsim 3$. A few exceptions come from studies that estimated n_e based on doubly-ionized regions, such as Killi et al. (2023) who observed a galaxy at $z = 7.133$ with Atacama Large Millimeter Array (ALMA) and estimated $n_e \lesssim 500 \text{ cm}^{-3}$ based on the [O III] $\lambda 52 \mu\text{m}/[\text{O III}] \lambda 88 \mu\text{m}$ ratio. However, this diagnostic probes a very different ISM region (i.e., dust-obscured) and ionization level compared to the [O II] $\lambda\lambda 3726, 3729$ and [S II] $\lambda\lambda 6716, 6731$ doublets.

After the launch of JWST, several studies have already explored n_e out to $z \sim 9$ using various diagnostics. Isobe et al. (2023) used the spectroscopic data from public JWST surveys to measure n_e of 14 galaxies at $z = 4.02 - 8.68$. Among the sample, only three galaxies (with the highest $z = 7.87$) observed with NIRSpec high-resolution grating by the GLASS survey (Treu et al. 2022) showed resolved [O II] $\lambda\lambda 3726, 3729$ doublet, while the doublet remains unresolved in the rest of the sample. They estimated $n_e \gtrsim 300 \text{ cm}^{-3}$. Reddy et al. (2023) investigated the connections between the ionization parameter (U), electron density

* Hubble Fellow

† NASA Postdoctoral Fellow

(n_e), and star formation rate (SFR) based on 48 galaxies at $2.7 < z < 6.3$. They measured n_e based on the [S II] $\lambda\lambda 6716, 6731$ doublet resolved in NIRSpec medium-resolution spectra from the Cosmic Evolution Early Release Science (CEERS; Finkelstein et al. 2023; Fujimoto et al. 2023). They found that galaxies with higher $O32 = [\text{O III}] \lambda 4959, \lambda 5007 / [\text{O II}] \lambda \lambda 3726, 3729$ have average $n_e \simeq 500 \text{ cm}^{-3}$ that are $\gtrsim 5$ times larger than that of lower- $O32$ galaxies. They also found a highly significant positive correlation between U and SFR surface density (Σ_{SFR}), which appears to be independent of redshift at $1.6 \lesssim z \lesssim 6.3$.

While JWST/NIRSpec prism spectroscopy cannot resolve [O II] $\lambda\lambda 3726, 3729$ and [S II] $\lambda\lambda 6716, 6731$ lines due to low spectral resolution ($R \sim 30 - 300$), some studies have combined [O III] $\lambda 5007$ observed by this instrument with [O III] $\lambda 88 \mu\text{m}$ observed with ALMA to indirectly estimate n_e of galaxies at $z = 9.11$ ($\sim 400 \text{ cm}^{-3}$; Stiavelli et al. 2023) and $z = 8.496$ ($\sim 220 \text{ cm}^{-3}$; Fujimoto et al. 2022) using photoionization modeling. Until now, no studies have directly measured n_e from resolved [O II] $\lambda\lambda 3726, 3729$ doublet at $z > 8$, while [S II] $\lambda\lambda 6716, 6731$ is redshifted beyond the wavelength coverage of NIRSpec. The detection of [O II] $\lambda\lambda 3726, 3729$ doublet remains challenging because most galaxies at such high redshift are faint. Moreover, high resolution ($R > 2000$) spectroscopy is needed to be able to resolve the doublets, which is only achievable using the NIRSpec high-resolution grating. Recently, the [O II] $\lambda\lambda 3726, 3729$ doublet has been observed in the spectrum of GN-z11 by Bunker et al. (2023), one of the brightest galaxies known at $z > 10$ (Oesch et al. 2016; Tacchella et al. 2023). However, the NIRSpec medium-resolution grating cannot resolve the single lines.

In this paper, we present NIRSpec high-resolution ($R \sim 2700$) spectroscopy of MACS0647–JD, a triply-lensed galaxy at $z = 10.167$ (Coe et al. 2013; Hsiao et al. 2023b,a). Previously, JWST/NIRCam imaging and NIRSpec prism spectroscopy have been obtained for this galaxy by GO 1433 (PI Coe). The NIRCam imaging resolved the galaxy into two components A and B, suggesting a possible galaxy merger (Hsiao et al. 2023b). NIRSpec prism spectra of JD1 and JD2 (the two brightest lensed images of MACS0647–JD) were presented in Hsiao et al. (2023a), revealing 7 strong emission lines and becoming one of the highest redshift galaxies with detected rest-frame UV emission lines besides GHZ2/GLASS-z12 (Castellano et al. 2024), GN-z11 (Bunker et al. 2023), and JADES-GS-z11-0 (Hainline et al. 2024). Here, we observe JD1 and JD2 with the high-resolution G395H/F290LP setting to further resolve the lines and obtain better measurements of their

fluxes and widths. We resolve [O II] $\lambda\lambda 3726, 3729$ doublet for the first time at $z > 8$ and use it to estimate n_e .

The paper is organized as follows. We describe the NIRSpec data and its reduction in Section 2. The measurements of emission lines are described in Section 3. We present and discuss our results in Section 4, and finally conclude in Section 5. Throughout, we assume the cosmological parameters of $\Omega_m = 0.3$, $\Omega_\Lambda = 0.7$, and $H_0 = 70 \text{ km s}^{-1} \text{ Mpc}^{-1}$.

2. DATA

2.1. NIRSpec MSA Spectroscopy

The NIRSpec micro-shutter assembly (MSA) Spectroscopy Ferruit et al. (2022) observation was conducted on January 14, 2024, as part of GO 4246 (PI Abdurro’uf), which focuses on MACS0647–JD at $z = 10.17$. We use the high-resolution grating G395H/F290LP that covers a wavelength range of 2.87–5.14 μm with spectral resolution ranges from $R \sim 1900$ to 3500 over the wavelength range. The total exposure time was 2.43 hours. Half of that time was observed with standard 3-slitlet nods. With the other half, we used single slitlets and performed two dithers. The slitlets on JD1 and JD2 mainly cover the brightest Component A (see Figure 1). This is similar to the NIRSpec prism observation previously performed (Hsiao et al. 2023a). The data are all publicly available on MAST, but not the reduction we analyzed in this paper which will be described below.¹

2.2. NIRSpec Data Reduction

The data were reduced with the JWST pipeline using CRDS version 11.17.6 and `jwst_1183.pmap` with the 2D spectra obtained from the Mikulski Archive for Space Telescopes (MAST). The 2D frames were visually inspected for artifacts and the snowballs and residual cosmic rays were manually masked. Additional sigma clipping with a threshold of 6σ was then applied to the 2D spectra to remove any additional spurious pixels. The source’s one-dimensional (1D) spectra were obtained via an optimal extraction (Horne 1986) with a spatial weight profile from the trace of the source in the masked 2D spectrum such that the pixels near the peak of the trace are maximally weighted. To create the extraction profile, the 2D signal-to-noise (SNR) spectrum was collapsed in the spectral direction, taking the median value at each spectral pixel and fitting a Gaussian to the positive trace. While the NIRSpec shutter includes flux from both Component A and Component B

¹ <https://mast.stsci.edu/search/ui/#/jwst>.

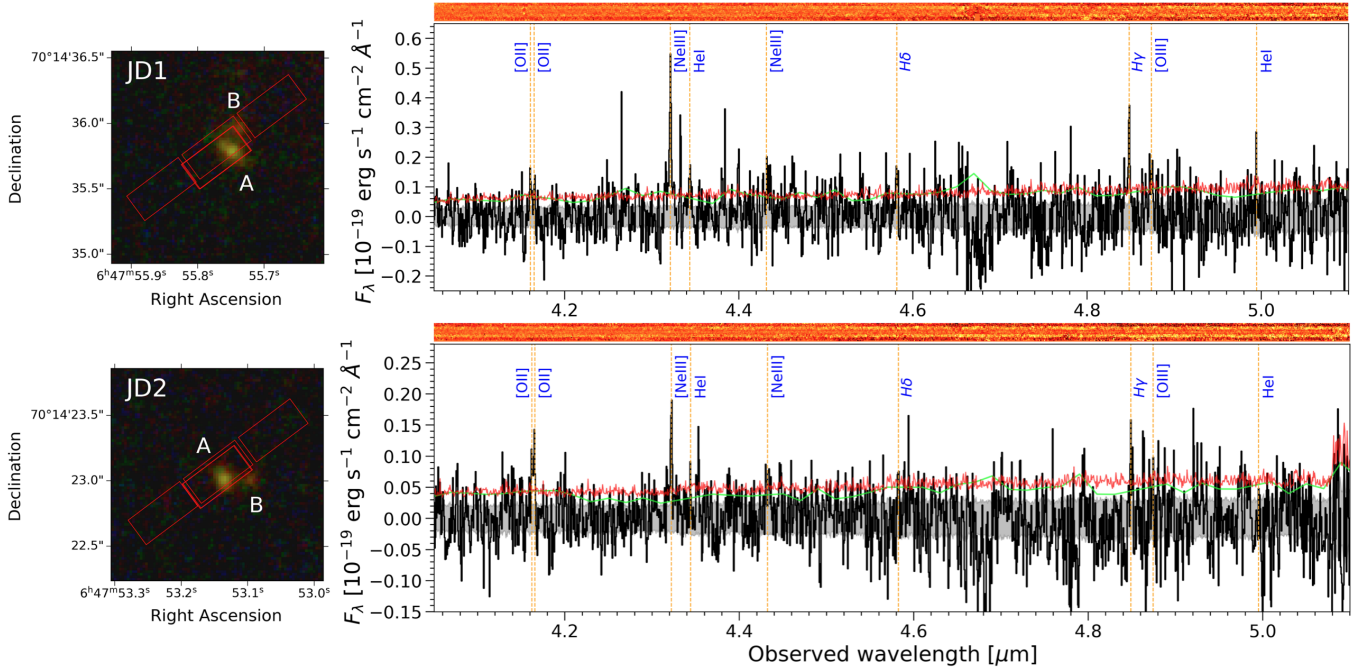


Figure 1. NIRSpect G395H/F290LP spectra of MACS0647–JD lensed images JD1 and JD2 (IDs 3593 and 3349, respectively, in the catalog used for preparing the observation). *Left panel:* Slitlet positions overlaid on $1.6'' \times 1.6''$ NIRCcam color images (blue:F115W; green:F150W; red:F200W). *Right panel:* 2D and 1D NIRSpect high-resolution spectra of JD1 (top) and JD2 (bottom). Several emission lines are detected while the continuum is not. Emission lines are indicated with blue-colored labels and orange vertical dashed lines. The gray shaded area represents the uncertainties obtained from the pipeline. The green lines represent the standard deviations of the spectral fluxes after removing the emission lines. We multiply the flux uncertainties by a factor of two to match the overall level of the standard deviations. This is shown with a red line. These rescaled uncertainties are used for the analysis in this paper.

for JD1 (ID 3593), the orientation is such that Component B falls completely out of the shutter for JD2 (ID 3349). The source is effectively spatially unresolved at all wavelengths (intrinsic size is less than the JWST point spread function full width at half maximum, PSF FWHM), and there was only a single detectable trace in both observations at the expected location of Component A. An attempt to extract a spectrum for both Component A and Component B from JD1 yielded no discernible detections for Component B, which was affected by the location of the upper negative trace in the 2D spectrum.

Figure 1 shows 2D and 1D spectra of JD1 (top right) and JD2 (bottom right) along with the slitlet positions overlaid on $1.6'' \times 1.6''$ NIRCcam color images (left). We detect several emission lines, including [O II] $\lambda\lambda 3726, 3729$ doublet, [Ne III] $\lambda 3870$, He I $\lambda 3890$, H δ , H γ , and [O III] $\lambda 4363$. However, we do not detect the spectral continuum. The positions of emission lines are indicated with orange dashed lines and blue labels. The gray shaded area represents the flux uncertainties produced by the pipeline. These uncertainties might be underestimated (see e.g., Ferruit et al. 2022; Christensen et al. 2023). Therefore, we check it by calculating the

standard deviations of the spectral fluxes after removing the emission lines ($\pm 50 \text{ \AA}$). The green lines in Figure 1 show the standard deviation level, which is higher by a factor of ~ 2 from the estimated flux uncertainties from the pipeline. The red lines represent the flux uncertainties multiplied by a factor of two, which we use for our analysis in this paper. The reprocessed spectra will be publicly available on our Cosmic Spring website².

3. ANALYSIS

Most of the emission lines that were previously detected with the NIRSpect prism data (see Hsiao et al. 2023a) are also detected with the current NIRSpect high-resolution data, except [C III] $\lambda 1907$ which is beyond the wavelength coverage of the current data. With the high-resolution grating, we can resolve [O II] $\lambda\lambda 3726, 3729$ doublet for the first time at $z > 8$. At the central wavelength of [O II] $\lambda\lambda 3726, 3729$, the G395H/F290LP grating has $R \sim 2855$ (Jakobsen et al. 2022) which corresponds to a rest-frame dispersion of $\sim 1.3 \text{ \AA}$ per spectral resolution element. Besides this, He I $\lambda 3890$ is separated from

² <https://cosmic-spring.github.io>

[Ne III] λ 3870, which were blended in the NIRSpec prism spectra. We describe the emission line analysis in this section.

3.1. Stacking and Emission Line Measurements

We stack (i.e., sum) the spectra of JD1 and JD2 to get a good overall S/N ratio. The stacked spectrum has a total lensing magnification (μ) of 13.3 ($8.0 + 5.3$; see Hsiao et al. 2023a,b). We do not de-lense the spectra of JD1 and JD2 before the stacking because the true line ratios of MACS0647–JD are expected to be preserved. We measure the emission line flux and width in the individual spectra (JD1 and JD2) and the stacked spectrum. We fit the emission lines individually with a Gaussian function using PIXEDFIT³ (Abdurro’uf et al. 2021, 2022, 2023). The code uses the Markov Chain Monte Carlo (MCMC) method through the EMCEE package (Foreman-Mackey et al. 2013) for sampling the posterior probability distributions of free parameters in the fitting.

First, we determine the systemic redshift by fitting the strongest line [Ne III] λ 3870 as it also has the highest S/N ratio. The spectroscopic redshift of MACS0647–JD has been previously determined by Hsiao et al. (2023a) using NIRSpec prism data to be 10.17. Here, we put a stronger constraint on the redshift using NIRSpec high-resolution data. We obtain $z = 10.1672_{-0.0003}^{+0.0003}$, $10.1685_{-0.0004}^{+0.0004}$, and $10.1674_{-0.0002}^{+0.0002}$ for JD1, JD2, and stacked spectrum, respectively. For each spectrum, we use the systemic redshift to estimate the observed central wavelength of the other emission lines and set the initial positions of the MCMC walkers. To better constrain the FWHM of the lines, we use the FWHM posterior distribution function derived from the fitting of [Ne III] λ 3870 as an additional prior. For [O II] $\lambda\lambda$ 3726,3729 doublet, we set the two lines to have the same FWHM, while the value is allowed to vary during the fitting process.

For each emission line, we fit the spectrum region within ± 100 Å around the expected peak wavelength to minimize the influence of noise. We estimate the continuum level by taking the median of fluxes within the fitting region after excluding the emission line (i.e., masked around ± 40 Å from the expected peak wavelength). We then subtract the continuum from the spectrum and fit the emission line. We scale up the flux uncertainties by a factor of two to match the overall level of the standard deviation (see Figure 1).

We do not use the measured continuum fluxes from the NIRSpec prisms spectra because of the differences in

the slitlet position and coverage. In Hsiao et al. (2023a), the measurements of emission lines were performed to a stacked spectrum, which is summed of the JD1 and JD2 spectra from two observations (Obs 21 and Obs 23). In Appendix C, we perform emission line measurements of the individual NIRSpec prism spectra and the stacked one using the updated reductions and fitting method.

3.2. Measured Emission Line Properties

We show the fitting results for the stacked spectrum, JD1, and JD2 in Figures 2, 3, and 4, respectively. Measured properties of the emission lines are summarized in Tables 1, 2, and 3. In each figure, the full spectrum is shown in the first row, while cutouts of emission lines are shown in the second and third rows. The red line and shaded area in each cutout show the Gaussian model drawn from the median posteriors and the range given by the 16th and 84th percentiles, respectively. For the [O II] $\lambda\lambda$ 3726,3729 doublet, the best fits of the individual lines are shown by the blue and green dashed lines, while the red line shows the total. The flux uncertainties shown in the cutout spectra have been scaled up by a factor of two.

We detect and resolve [O II] $\lambda\lambda$ 3726,3729 doublet with S/N of $\sim 3 - 4$ on the individual lines. The flux ratio between the two lines, $R_{[\text{O II}]} = [\text{O II}] \lambda 3729 / \lambda 3726$ are $0.71_{-0.22}^{+0.32}$, $1.04_{-0.30}^{+0.27}$, and $0.91_{-0.27}^{+0.29}$ for the JD1, JD2, and stacked spectrum, respectively. The flux ratios are consistent within their uncertainties, though the median values are slightly different. This is likely caused by the noise and the different slit coverage on JD1 and JD2 (see Figure 1). The stacked [O II] $\lambda\lambda$ 3726,3729 has an observed FWHM of 183_{-15}^{+15} km s⁻¹, or 150_{-19}^{+18} km s⁻¹ intrinsic after correcting for instrumental line broadening of 105 km s⁻¹.

The strongest line [Ne III] λ 3870 is detected with a high S/N of 11.2 and 6 in JD1 and JD2, while it is 16.6 in the stacked spectrum. The observed systemic FWHM from the stacked [Ne III] λ 3870 is 176_{-14}^{+16} km s⁻¹, or 144_{-17}^{+19} km s⁻¹ intrinsic after correcting for instrumental broadening of 101 km s⁻¹. The good detection of [Ne III] λ 3870 and [O II] $\lambda\lambda$ 3726,3729 allows us to measure $\text{Ne3O2} \equiv [\text{Ne III}] \lambda 3870 / [\text{O II}] \lambda\lambda 3726,3729$ ratio. From the NIRSpec high-resolution data, we obtain Ne3O2 of $2.1_{-0.4}^{+0.7}$, $0.7_{-0.2}^{+0.2}$, and $1.2_{-0.1}^{+0.2}$ for JD1, JD2, and stacked spectrum, respectively. We also determine Ne3O2 from NIRSpec prism data (see Appendix C) and obtain $1.2_{-0.4}^{+0.6}$, $1.0_{-0.2}^{+0.3}$, $1.1_{-0.1}^{+0.2}$, $1.7_{-0.3}^{+0.4}$ for the JD1 Obs 21, JD1 Obs23, JD2 Obs21, JD2 Obs23, respectively. Again, the discrepancies can be caused by the difference in the slit coverage and noise (in the case of the high-resolution data). Recent studies of high redshift

³ The line fitting function will be included in the future release of PIXEDFIT

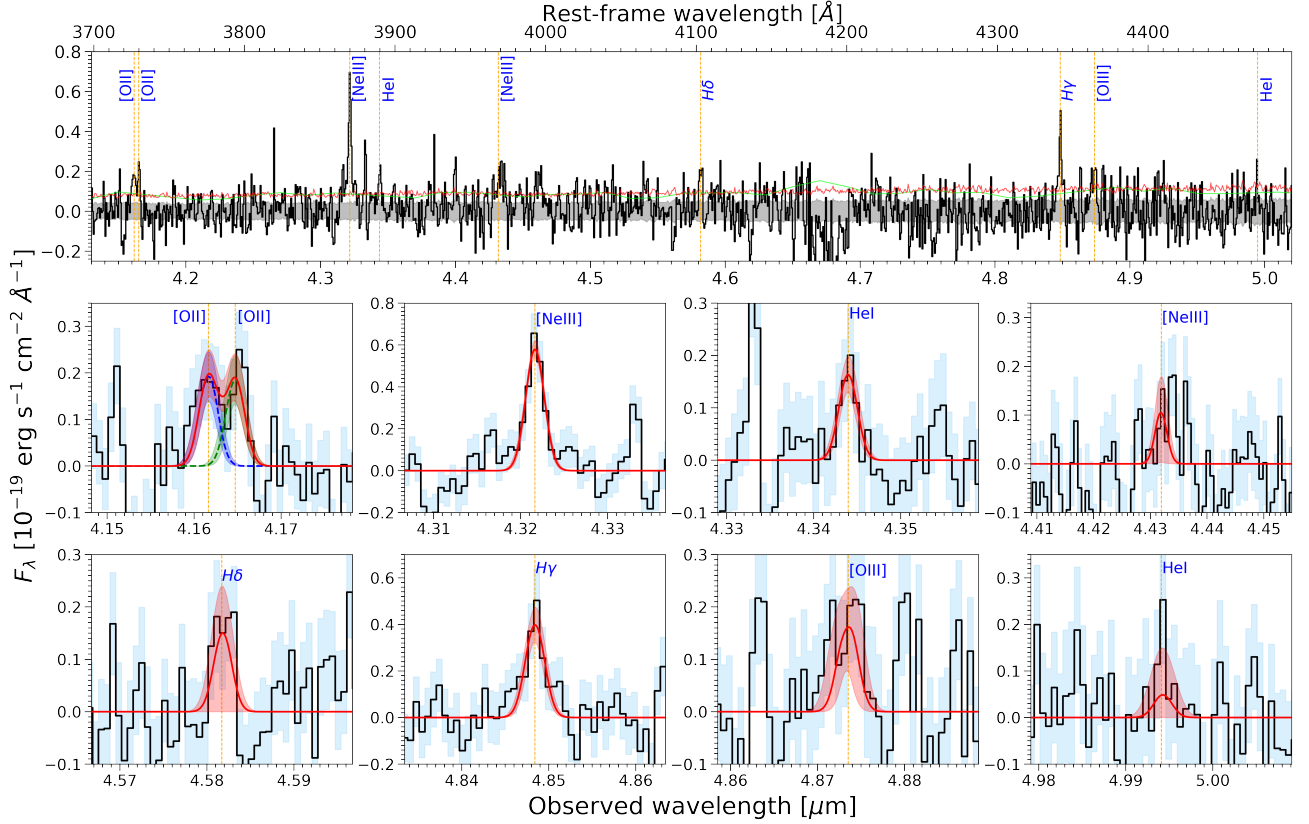


Figure 2. *Top:* Fitting results of the emission lines in the stacked spectrum. The gray shaded area shows the original flux uncertainties, while the red line represents a factor of two scale-up, which is used in the fitting. This matches with the overall level of standard deviations as shown by the green line. The detected emission lines are indicated with orange vertical dashed lines and blue labels. *Middle and bottom:* cutouts showing the detected emission lines and the best-fit Gaussian model drawn from the posteriors obtained from the MCMC fitting. The best-fit models are shown by the red lines (median) and red-shaded areas (range between 16th and 84th percentiles). The best fits of the individual [O II] $\lambda\lambda 3726, 3729$ lines are shown in blue and green, while the total is shown in red. The flux uncertainties in the cutouts have been scaled up by a factor of two.

($3 \lesssim z \lesssim 9$) galaxies using JWST/NIRSpec data measured Ne3O2 in the range of $\sim 0.2 - 3$ (e.g., Tang et al. 2023; Reddy et al. 2023; Cameron et al. 2023; Sanders et al. 2024; Backhaus et al. 2024), in agreement with the values determined for MACS0647–JD.

4. RESULT AND DISCUSSION

4.1. Measurement of Electron Density

We measure n_e from the line ratio $R_{[\text{OII}]}$ based on the photoionization models adopted from Kewley et al. (2019a), which were generated using the MAPPINGS version 5.1 photoionization code (Binette et al. 1985; Sutherland & Dopita 1993; Dopita et al. 2015). We

perform interpolations to the model grids from Kewley et al. (2019a) and construct a functional formula for converting $R_{[\text{OII}]}$ to n_e that takes into account the electron temperature (T_e). We describe this in detail in Appendix A.

Figure 5 shows the model $R_{[\text{OII}]}(n_e)$ curves for 9 values of T_e calculated using the constructed formula (Equations A1 and A2). Different electron temperatures are indicated with different colors. The vertical gray dashed lines mark the range of electron densities for which the line ratio is a useful density diagnostic according to Kewley et al. (2019a). The black dashed line shows the relation from Sanders et al. 2016 (Eq. 6 therein). It perfectly matches the curve from Kewley et al. (2019a) for $T_e = 10000$ K, which was indeed assumed in Sanders et al. (2016).

We use the new formula for calculating the n_e of MACS0647–JD system. From our fitting (see Sections 3.1 and 3.2), we obtain $R_{[\text{OII}]}$ of $0.71^{+0.32}_{-0.22}$,

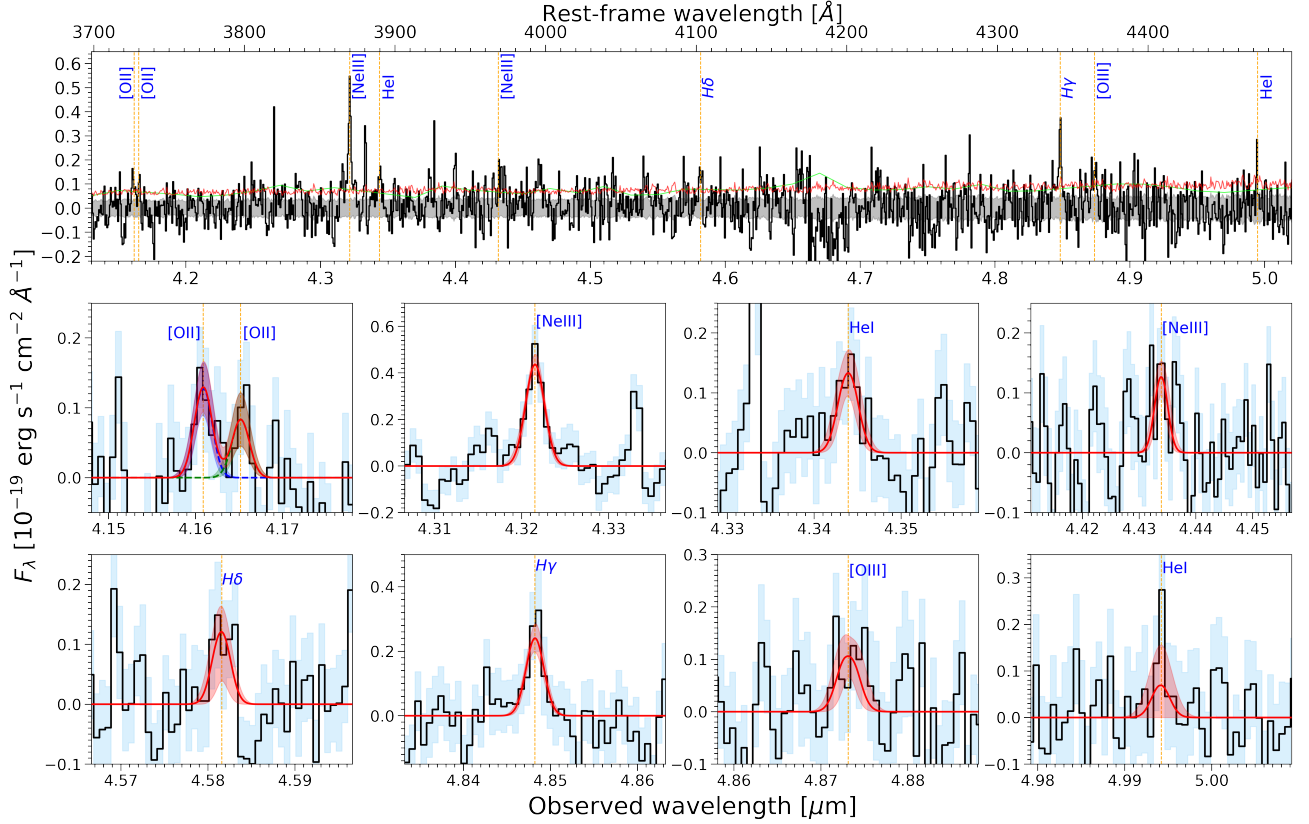


Figure 3. Same as Figure 2 but for JD1 spectrum.

$1.04^{+0.27}_{-0.30}$, and $0.91^{+0.29}_{-0.27}$ for the JD1, JD2, and stacked spectrum, respectively. Assuming $T_e = 17000$ K for MACS0647–JD as calculated in a companion paper (Hsiao et al., in prep.), we obtain electron densities of $\log(n_e/\text{cm}^{-3}) = 3.3^{+0.6}_{-0.5}$, $2.7^{+0.5}_{-0.6}$, and $2.9^{+0.5}_{-0.5}$, respectively. In Figure 5, those values are indicated with blue, red, and black circles, respectively. With the current measured $R_{[\text{OII}]}$, we check that changing the assumptions of electron temperature from $T_e = 10000$ to 30000 K increases n_e by a factor of ~ 1.7 .

We also estimate n_e using PYNEB (Luridiana et al. 2015) task `getCrossTemDen` and combine measured $R_{[\text{OII}]}$ from the stacked spectrum and $[\text{O III}]\lambda 5007/\lambda 4363 = 40 \pm 5$ line ratio measured in a companion paper (Hsiao et al., in prep.). We obtain $\log(n_e) = 2.9^{+0.3}_{-0.4}$, which is consistent with the value derived above.

We highlight the fitting results of $[\text{O II}]\lambda\lambda 3726, 3729$ in Figure 6. Even though JD1 and JD2 are lensed images of the same galaxy, there is an opposite trend of $R_{[\text{OII}]}$ between JD1 and JD2 if we examine the median values. However, they are consistent within the range given their uncertainties. With the MCMC method performed here, we propagate the uncertainty from the

spectra to the posterior probability distribution of n_e in a self-consistent way. We show the posterior distributions of n_e (along with the fluxes of the two lines in $[\text{O II}]\lambda\lambda 3726, 3729$ doublet, and FWHM) in Appendix B (Figure 9). The posteriors of these parameters are converged, indicating a good fitting. The apparent cut (i.e., envelope) in the 2D posterior between the two line fluxes is due to the range given by the $R_{[\text{OII}]}$ within which n_e is physically realistic. From the Equations A1 and A2, this range is between 0.3729 and 1.4556 for $T_e = 17000$ K. We note that this range is not imposed from the beginning (i.e., in the fitting process).

$R_{[\text{OII}]}$ is also a good indicator of the ISM pressure, which is defined as the pressure within the ionized gaseous nebulae surrounding young hot stars (e.g., Kewley et al. 2019a). Using the photoionization models of Kewley et al. (2019a, Figure 10 therein) and assuming $12 + \log(\text{O}/\text{H}) = 7.79 \pm 0.09$ (Hsiao et al., in prep.), we estimate ISM pressure of $\log(P/\text{k}) = 7.3^{+0.4}_{-0.3}$.

4.2. Redshift evolution of n_e

Here, we put the measured electron density of MACS0647–JD into the context of galaxy evolution by comparing it with the measurements at lower redshifts.

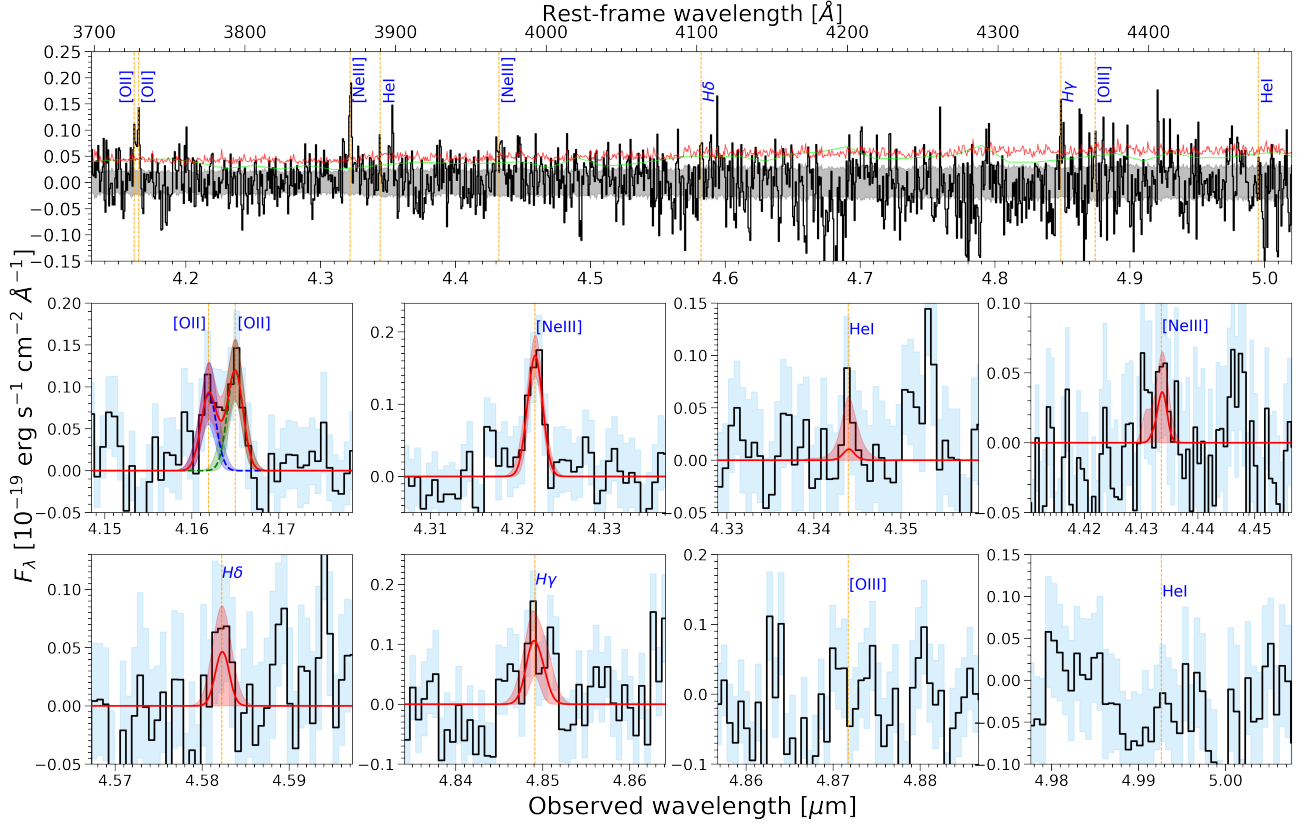


Figure 4. Same as Figure 2 but for JD2 spectrum. The fitting results of [O III] $\lambda 5007$ and HeI $\lambda 4473$ are omitted because of the insignificant detection of the lines.

We compile measured electron densities at $z = 0 - 9$ reported in the literature and plot them in Figure 7. Different symbols represent various emission-line diagnostics used in deriving n_e , while different colors represent different studies. Three emission-line diagnostics have been used in the literature to derive n_e : $R_{[\text{OII}]}$ (square), $R_{[\text{SII}]}$ (plus), and an indirect method using [O III] $\lambda 88\mu\text{m}/\lambda 5007$ ratio (cross). Some observations do not resolve [O II] $\lambda\lambda 3726, 3729$ doublet because of the insufficient spectral resolution. We indicate the results from those studies with open squares. For studies that reported n_e of the individual galaxies, we show those values with transparent symbols, in addition to the median values shown with thick symbols. The measured n_e of JD1, JD2, and stacked spectrum are shown with the blue, red, and black squares, respectively. The rest of the data points are listed in the following, classified based on the redshift range.

- $z \lesssim 0.2$: Berg et al. (2022) measured n_e of 45 local star-forming galaxies at $0.002 < z < 0.182$ using data from the CLASSY survey (Berg et al. 2022; James et al. 2022). They derived n_e based on $R_{[\text{SII}]} = [\text{S II}] \lambda 6716 / \lambda 6731$ and obtained a wide

range of $n_e \sim 10 - 900 \text{ cm}^{-3}$, with a median of 100 cm^{-3} . Using the same CLASSY sample, Mingozi et al. (2022) explored multiple UV diagnostics for measuring the properties of ISM, including n_e , in which they applied multiple line ratios representing low- and high-ionization regions. We take n_e measured based on $R_{[\text{SII}]}$ whose T_e is derived based on [O III] $\lambda 4363 / \lambda 5007$. Davies et al. (2021) measured n_e of galaxies in a wide redshift range by stacking the spectra of the galaxies in four redshift bins: $z \lesssim 0.1$ (471), $0.6 \lesssim z \lesssim 1.1$ (39), $1.1 \lesssim z \lesssim 1.9$ (36), and $1.9 \lesssim z \lesssim 2.6$ (65). The data for local galaxies are taken from SAMI survey (Croom et al. 2012). They estimated $n_e = 32^{+4}_-9 \text{ cm}^{-3}$ from $R_{[\text{SII}]}$. Kashino et al. (2017) and Kaasinen et al. (2017) measured n_e of galaxies at $z \sim 1.5$ and $z \sim 0$. For the local sample, they used data from the SDSS Data Release 7 (Abazajian et al. 2009), specifically the MPA-JHU catalogs (Kauffmann et al. 2003; Brinchmann et al. 2004). For the local sample, Kaasinen et al. (2017) obtained a median of $n_e = 26.8^{+0.2}_{-0.2} \text{ cm}^{-3}$, while Kashino et al. (2017) obtained n_e in the range of $\sim 10 - 100$

Table 1. Measured Emission Line Properties of the stacked Spectrum

Emission Line	Rest wavelength (Å)	Observed wavelength (μm)	Observed Flux ^a (10^{-20} erg s ⁻¹ cm ⁻²)	S/N	Observed FWHM ^b (km s ⁻¹)
[O II]	3727.10	4.16165 ^{+0.00035} _{-0.00039}	55 ⁺¹⁴ ₋₁₄	3.9	183 ⁺¹⁵ ₋₁₅
[O II]	3729.86	4.16473 ^{+0.00036} _{-0.00039}	53 ⁺¹⁴ ₋₁₄	3.9	183 ⁺¹⁵ ₋₁₅
[Ne III]	3869.86	4.32164 ^{+0.00007} _{-0.00007}	157 ⁺¹⁰ ₋₉	16.6	176 ⁺¹⁶ ₋₁₄
He I	3889.75	4.34396 ^{+0.00028} _{-0.00030}	45 ⁺⁹ ₋₉	5.0	173 ⁺¹⁵ ₋₁₅
[Ne III]	3968.59	4.43192 ^{+0.00025} _{-0.00050}	29 ⁺²¹ ₋₂₉	1.4	177 ⁺³⁷ ₋₁₇
H δ	4102.89	4.58172 ^{+0.00061} _{-0.00126}	45 ⁺²³ ₋₃₅	1.8	162 ⁺¹⁵ ₋₁₁
H γ	4341.69	4.84842 ^{+0.00025} _{-0.00027}	113 ⁺²⁰ ₋₂₀	5.7	162 ⁺¹³ ₋₁₃
[O III]	4364.44	4.87352 ^{+0.00085} _{-0.00113}	58 ⁺¹⁸ ₋₁₉	3.1	159 ⁺¹³ ₋₁₄
He I	4472.74	4.99409 ^{+0.00151} _{-0.00560}	24 ⁺²³ ₋₁₈	1.3	151 ⁺¹³ ₋₁₅

^aMeasured fluxes from the observed spectrum that have not been corrected for a lensing magnification. The stacked spectrum has the total magnification of $\mu = 13.3$ ($8.0 + 5.3$).

^bObserved FWHM before correcting for the instrumental broadening.

Table 2. Measured Emission Line Properties of the JD1 Spectrum

Emission Line	Rest wavelength (Å)	Observed wavelength (μm)	Observed Flux ^a (10^{-20} erg s ⁻¹ cm ⁻²)	S/N	Observed FWHM ^b (km s ⁻¹)
[O II]	3727.10	4.16086 ^{+0.00030} _{-0.00034}	34 ⁺⁹ ₋₁₀	3.3	175 ⁺²⁴ ₋₂₂
[O II]	3729.86	4.16517 ^{+0.00030} _{-0.00034}	23 ⁺¹⁰ ₋₉	2.4	175 ⁺²⁴ ₋₂₂
[Ne III]	3869.86	4.32154 ^{+0.00010} _{-0.00011}	121 ⁺¹¹ ₋₁₁	11.2	180 ⁺²⁵ ₋₂₂
He I	3889.75	4.34390 ^{+0.00046} _{-0.00051}	41 ⁺¹¹ ₋₁₁	3.8	184 ⁺²³ ₋₂₂
[Ne III]	3968.59	4.43389 ^{+0.00048} _{-0.00045}	39 ⁺⁹ ₋₉	3.4	188 ⁺²⁵ ₋₂₃
H δ	4102.89	4.58160 ^{+0.00073} _{-0.00038}	34 ⁺¹¹ ₋₁₇	2.2	162 ⁺²⁰ ₋₁₅
H γ	4341.69	4.84823 ^{+0.00015} _{-0.00018}	63 ⁺⁹ ₋₉	7.0	152 ⁺¹⁸ ₋₁₈
[O III]	4364.44	4.87314 ^{+0.00095} _{-0.00070}	37 ⁺¹¹ ₋₁₁	3.4	167 ⁺²⁰ ₋₂₁
He I	4472.74	4.99419 ^{+0.00229} _{-0.00138}	26 ⁺²⁰ ₋₁₉	1.5	152 ⁺²² ₋₂₀

^aMeasured fluxes from the observed spectrum that have not been corrected for a lensing magnification, which is $\mu = 8$ for JD1.

^bObserved FWHM before correcting for the instrumental broadening.

cm⁻³. Shirazi et al. (2014) studied the ISM properties in 14 star-forming galaxies at $2.6 < z < 3.4$ and local galaxies matched in stellar mass and sSFR. They used emission lines from the MPA-JHU catalogs for the local sample, and estimated n_e based on $R_{[\text{SII}]}$, finding a range of $\sim 60 - 250$ cm⁻³.

- $0.2 \lesssim z \lesssim 4$: Davies et al. (2021) used data from the KMOS^{3D} survey (Wisnioski et al. 2015) to measure n_e of galaxies in 3 high- z bins (mentioned above). Based on the $R_{[\text{SII}]}$ of the stacked

spectra, they estimated $n_e = 101_{-85}^{+59}$, 79_{40}^{+120} , and 187_{-132}^{+140} cm⁻³ for the samples at $z \sim 0.9$, ~ 1.5 , and ~ 2.2 , respectively. Swinbank et al. (2019) used data from the KROSS survey (Stott et al. 2016) and performed stacking on the spectra of 529 star-forming galaxies at $0.6 < z < 1.0$. They estimated n_e from $R_{[\text{SII}]}$ in the stacked spectrum and decomposed it into broad-line and narrow-line components. They estimated $n_e = 30_{-20}^{+40}$ and 75_{-50}^{+55} cm⁻³ for the narrow-line and broad-line components, respectively. We take the mean

Table 3. Measured Emission Line Properties of the JD2 Spectrum

Emission Line	Rest wavelength (Å)	Observed wavelength (μm)	Observed Flux ^a (10 ⁻²⁰ erg s ⁻¹ cm ⁻²)	S/N	Observed FWHM ^b (km s ⁻¹)
[O II]	3727.10	4.16192 ^{+0.00032} _{-0.00035}	22 ⁺⁸ ₋₈	2.8	156 ⁺³⁷ ₋₃₁
[O II]	3729.86	4.16500 ^{+0.00032} _{-0.00035}	29 ⁺⁸ ₋₈	3.4	156 ⁺³⁷ ₋₃₁
[Ne III]	3869.86	4.32203 ^{+0.00016} _{-0.00017}	37 ⁺⁶ ₋₆	6.0	143 ⁺³³ ₋₂₅
He I	3889.75	4.34394 ^{+0.00172} _{-0.00327}	7 ⁺⁷ ₋₅	1.2	130 ⁺⁴⁷ ₋₅₀
[Ne III]	3968.59	4.43354 ^{+0.00064} _{-0.00246}	11 ⁺⁵ ₋₆	1.9	149 ⁺⁴⁴ ₋₄₆
Hδ	4102.89	4.58226 ^{+0.00074} _{-0.00091}	12 ⁺⁸ ₋₉	1.6	125 ⁺⁴² ₋₃₂
Hγ	4341.69	4.84911 ^{+0.00082} _{-0.00057}	30 ⁺¹² ₋₁₂	2.5	144 ⁺³⁹ ₋₄₃
[O III]	4364.44	4.87172 ^{+0.00278} _{-0.00149}	6 ⁺⁴ ₋₄	1.4	102 ⁺⁴⁴ ₋₃₉
He I	4472.74	4.34394 ^{+0.00172} _{-0.00327}	7 ⁺⁷ ₋₅	1.2	130 ⁺⁴⁷ ₋₅₀

^a Measured fluxes from the observed spectrum that have not been corrected for a lensing magnification, which is $\mu = 5.3$ for JD2.

^b Observed FWHM before correcting for the instrumental broadening.

of the two for our analysis. Kashino et al. (2017) used data from the FMOS-COSMOS survey (Silverman et al. 2015) to study the ISM properties of galaxies at $1.4 \lesssim z \lesssim 1.7$. They measured an average $n_e = 220^{+170}_{-130} \text{ cm}^{-3}$ based on $R_{[\text{SII}]}$. Kaasinen et al. (2017) measured n_e of 21 star-forming galaxies at $1.4 \lesssim z \lesssim 1.7$ using data from the COSMOS-[OII] survey. The estimated n_e based on $R_{[\text{OII}]}$ ranges from ~ 9 to 1000 cm^{-3} , with a median of $114^{+28}_{-27} \text{ cm}^{-3}$. Harshan et al. (2020) used data from the ZFIRE survey (Nanayakkara et al. 2016) to calculate n_e of $z \sim 1.5$ galaxies, of which 6 are in the cluster environment and 2 are in the field. They found n_e in the range of $\sim 57 - 490 \text{ cm}^{-3}$ for the cluster galaxies and $\sim 49 - 160 \text{ cm}^{-3}$ for the field galaxies. Sanders et al. (2016) measured n_e of 97 galaxies at $2.0 < z < 2.6$ using data from the MOSDEF survey (Kriek et al. 2015). They obtained a median $n_e = 225^{+119}_{-4} \text{ cm}^{-3}$ based on $R_{[\text{OII}]}$. Steidel et al. (2014) estimated $n_e = 220^{+380}_{-160} \text{ cm}^{-3}$ from $R_{[\text{OII}]}$ of a stacked spectrum of 113 galaxies at $2.0 < z < 2.6$. Shimakawa et al. (2015) measured n_e of 14 H α -emitting galaxies at $z \sim 2.5$ based on $R_{[\text{OII}]}$. They obtained a median of $n_e \sim 290 \text{ cm}^{-3}$. Gburek et al. (2019) measured $n_e \sim 220 \text{ cm}^{-3}$ in a lensed dwarf galaxy at $z = 2.59$ based on $R_{[\text{OII}]}$. Onodera et al. (2016) derived n_e of star-forming galaxies at $3 \lesssim z \lesssim 3.7$ based on $R_{[\text{OII}]}$, finding a median $\sim 420 \text{ cm}^{-3}$. Shirazi et al. (2014) obtained $n_e \sim 110 - 2700 \text{ cm}^{-3}$ in star-forming galaxies at $2.6 < z < 3.4$ based on $R_{[\text{SII}]}$.

- $4 \lesssim z \lesssim 9$: Isobe et al. (2023) estimated n_e of 14 star-forming galaxies at $4.02 < z < 8.68$ using data from public JWST surveys that used the NIRSspec medium- and high-resolution spectroscopy. They observed [O II] $\lambda\lambda 3726, 3729$ doublet resolved in only three galaxies, but blended in the other galaxies. They carefully modeled the line spread function (LSF) of the NIRSspec to deconvolve the [O II] $\lambda\lambda 3726, 3729$ doublets. They obtained n_e range of $\sim 39 - 3100 \text{ cm}^{-3}$. Larson et al. (2023) studied the ISM properties in a galaxy CEERS_1019 at $z = 8.679$ using NIRSspec medium-resolution data. They carefully fit an unresolved [O II] $\lambda\lambda 3726, 3729$ doublet with two Gaussian models and derived $n_e = 1.9 \pm 0.2 \times 10^3 \text{ cm}^{-3}$. Fujimoto et al. (2022) measured n_e of a galaxy at $z = 8.496$ using indirect method based on the [O III] $88\mu\text{m}/\lambda 5007$ line ratio and obtained $n_e = 220^{+230}_{-130} \text{ cm}^{-3}$. Using the same method as Fujimoto et al. (2022), Stiavelli et al. (2023) estimated n_e of MACS1149-JD1 at $z = 9.11$ to be $\log(n_e) = 2.60^{+0.25}_{-0.27}$. With the [S II] $\lambda\lambda 6716, 6731$ doublets, Fujimoto et al. (2024) evaluated n_e of a sub- L^* main-sequence lensed galaxy at $z = 6.07$, *the Cosmic Grapes*, to be $n_e = 260^{+400}_{-230} \text{ cm}^{-3}$.

As shown in Figure 7, there is a clear trend of increasing n_e with redshift from $z = 0$ to 10. To get a functional form out of the evolutionary trend, we fit the data with a power-law function in the form of $n_e = A \times (1 + z)^p$ using the MCMC method. For the literature that reports electron densities of multiple individual galaxies in a redshift bin, we only use the median value for the

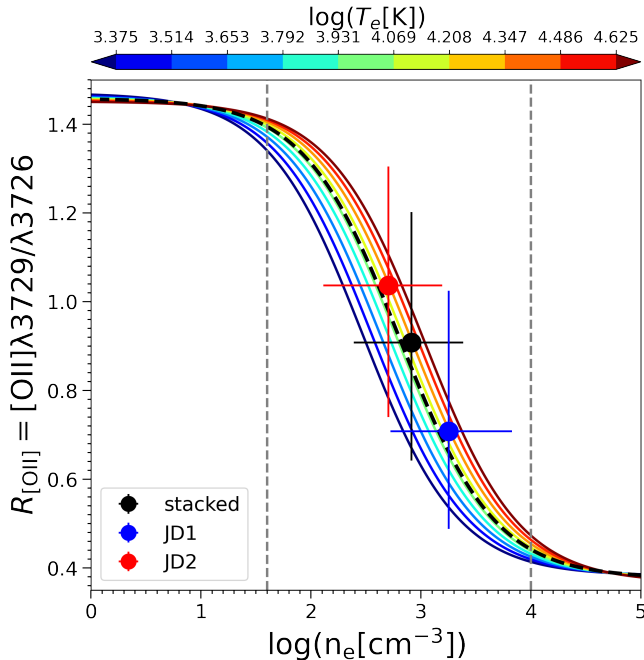


Figure 5. The relationship between $[\text{O II}] \lambda 3729/\lambda 3726$ and the electron density drawn from the photoionization models generated by Kewley et al. (2019a). The curves for different temperatures are shown with different colors. Equations A1 and A2 give the formulas to reconstruct these curves. The black dashed line represents the model from Sanders et al. (2016), which perfectly matches the Kewley et al. (2019a) model for $T_e = 10000$ K. The vertical gray dashed lines mark the range of electron densities for which the line ratio is a useful density diagnostic according to Kewley et al. (2019a). Given the $[\text{O II}] \lambda 3729/\lambda 3726$ line ratio and measured $T_e = 17000$ K (Hsiao et al., in prep.), the estimated n_e of JD1, JD2, and the stacked spectrum are shown by the red, blue, and black circles, respectively.

fitting. For MACS0647–JD, we only use the electron density derived from the stacked spectrum. We obtain $A = 54^{+31}_{-22} \text{ cm}^{-3}$ and $p = 1.2^{+0.4}_{-0.4}$. The median function obtained from the fitting result is shown with the black dashed line, while the gray shaded area shows 2σ uncertainty. The fitting result can track the bulk of the data distribution quite well. Best-fit A suggests an electron density of $\sim 50 \text{ cm}^{-3}$ in the local universe. The n_e of JD1, JD2, and stacked spectrum falls within the range of the best-fit line and 2σ uncertainty.

Previous studies have also hinted at a redshift evolution of electron density in the form of a power-law function, $n_e \propto (1+z)^p$ with $p \sim 1-2$ (e.g., Davies et al. 2021; Isobe et al. 2023). Isobe et al. (2023) compiled electron densities reported from the literature at $z \lesssim 3$ and combined with their measurements at $4 \lesssim z \lesssim 9$. They found that the majority of the data lie within the range given by the power-law function with $p = 1$ and

2. They further investigate the dependence of n_e on the M_* , SFR, and sSFR, and found that n_e seems to increase toward higher redshift at a given M_* , SFR, and sSFR, suggesting that n_e evolution is not an implication of the evolution of those global properties. This somewhat contradicts the finding of Kaasinen et al. (2017) that shows a weak evolution of n_e with redshift for a given SFR, suggesting that the redshift evolution of n_e is mainly due to the cosmic evolution of SFR. To further investigate the driving factors of n_e evolution, we need more data that cover a wide range of redshift and homogeneous methods in the measurements of the physical properties, which is beyond the scope of our current study. We do not investigate the dependence of n_e on the global properties of galaxies because of the inhomogeneity of the methods for deriving those properties used in the literature.

The values $n_e \approx 10^3 \text{ cm}^{-3}$ measured in JD1 and JD2 are in good agreement with the typical density of the ISM in the vicinity of massive stars, within star-forming regions, found in cosmological simulations of $z \sim 10$ galaxies (e.g., see Fig. 12 in Sugimura et al. 2024). However, understanding the dominant driver of the redshift evolution of n_e is more complicated. Although the mean density of the IGM and virialized halos scale as $(1+z)^3$, the phase of the ISM probed by the $[\text{O II}] \lambda \lambda 3726, 3729$ emission is ionized gas around newly formed massive stars, which is several orders of magnitude denser than the mean gas density in halos. One intriguing interpretation of the redshift evolution of n_e is in terms of the mean metallicity evolution of galaxies with redshift. This suggestion is based on two observations: i) Simulations of high-redshift galaxies find that the mean density of star-forming clumps roughly scales as $\bar{n} \propto Z^{-1}$, a result that is a direct consequence of their higher temperatures in lower-metallicity gas clouds (see Fig. 3 in Garcia et al. 2023); ii) The mean metallicity of the ISM in star-forming galaxies at redshifts $z \sim 0-3$, according to simulations (Davé et al. 2011) and observations (Yuan et al. 2012), decreases with increasing redshift roughly as $Z \propto (1+z)^{-1}$, hence the relationship $n_e \propto \bar{n} \propto (1+z)$.

Alternatively, the n_e evolution in the form of $n_e \propto (1+z)^p$ may be related to the morphological evolution of galaxies which influences the density of the ISM. The increasing ISM density toward high redshift can be caused by the size evolution of galaxies, which are more compact at high redshift. The galaxy size has been shown to decrease with redshift in the form of $r \propto (1+z)^{-1}$ (e.g., Shibuya et al. 2015; Ono et al. 2023; Ormerod et al. 2024). The virial radius of the dark matter halo also evolves at a similar rate (e.g., Mo & White 2002). Assuming disk morphology, which is

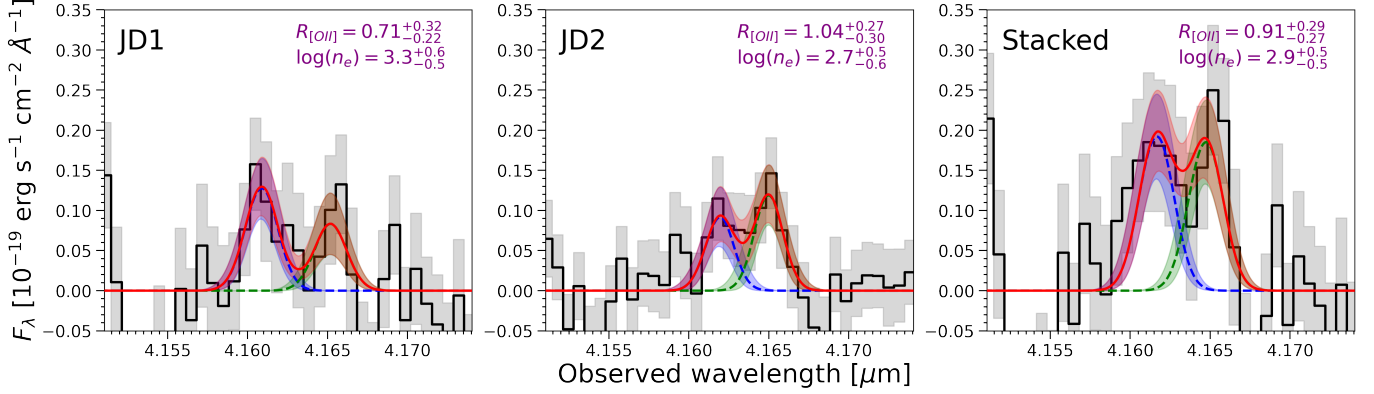


Figure 6. Resolved [O II] $\lambda\lambda 3726, 3729$ doublet of JD1 (left), JD2 (middle), and the stacked spectrum (right). The two lines are resolved in the three spectra. Green dashed and blue dashed lines are the best-fit Gaussian of [O II] $\lambda 3726$ and [O II] $\lambda 3729$ respectively, while the solid red line represents the total. Derived $R_{[\text{OII}]}$ of JD1, JD2, and stacked spectrum are $0.71^{+0.32}_{-0.22}$, $1.04^{+0.27}_{-0.30}$, and $0.91^{+0.29}_{-0.27}$, respectively. Assuming $T_e = 17000$ K (Hsiao et al., in prep.), we estimate n_e of $\log(n_e) = 3.3^{+0.6}_{-0.5}$, $2.7^{+0.5}_{-0.6}$, and $2.9^{+0.6}_{-0.5}$, respectively.

compatible with star-forming galaxies, the densities of stellar mass and dark matter halo mass are expected to evolve as $r^{-2} \propto (1+z)^{-2}$. If n_e is expected to evolve following the stellar mass and halo mass densities, it evolves as $n_e \propto (1+z)^{-2}$. Our result suggests a slightly lower power index of $1.2^{+0.5}_{-0.4}$.

5. SUMMARY

We present JWST/NIRSpec high-resolution spectroscopy (G395H/F290LP grating) of MACS0647–JD, a triply-lensed galaxy system at $z = 10.167$. We obtained spectra for the MACS0647–JD1 and –JD2. The new spectra detect and resolve emission lines in the rest-frame ultraviolet (UV) and blue optical, including resolved [O II] $\lambda\lambda 3726, 3729$ doublet, [Ne III] $\lambda 3870$, He I $\lambda 3890$, H δ , H γ , and [O III] $\lambda 4363$. The [O II] $\lambda\lambda 3726, 3729$ is resolved for the first time at $z > 8$, revealing the two lines and providing an unprecedented opportunity to directly measure electron density (n_e) in a galaxy at early cosmic time. We stack the spectra of JD1 and JD2 to get a higher overall signal-to-noise ratio. We measure n_e from the [O II] $\lambda 3729/\lambda 3726$ and obtained $\log(n_e/\text{cm}^{-3}) = 3.3^{+0.6}_{-0.5}$, $2.7^{+0.5}_{-0.6}$, and $2.9^{+0.5}_{-0.5}$ for JD1, JD2, and stacked spectrum, respectively. We compare our n_e measurements with those reported in the literature for galaxies in lower redshifts and study the evolutionary trend of n_e . We see a clear trend of increasing n_e with redshift. The redshift evolution follows a power-law function in the form of $n_e = A \times (1+z)^p$ with $A = 54^{+31}_{-22} \text{ cm}^{-3}$ and $p = 1.2^{+0.4}_{-0.4}$. This power-law form may be explained as the result of decreasing gas-phase metallicity of galaxies with increasing redshift, the morphological evolution of galaxies, or the combination of the two. It has been known that lower-metallicity star-forming clouds tend to be denser and the morpho-

logical evolution of galaxies happened in such a way that galaxies were more compact at higher redshift.

6. ACKNOWLEDGMENTS

This work is based on observations made with the NASA/ESA/CSA *James Webb Space Telescope* (JWST). The data were obtained from the Mikulski Archive for Space Telescopes (MAST) at the Space Telescope Science Institute (STScI), which is operated by the Association of Universities for Research in Astronomy (AURA), Inc., under NASA contract NAS 5-03127 for JWST. These observations are associated with programs JWST GO 4246 and 1433.

AA is funded by a grant for JWST-GO-01433 and JWST-GO-04246 provided by STScI under NASA contract NAS5-03127. TYYH appreciates the support from the Government scholarship to study abroad (Taiwan). We are grateful and indebted to the 20,000 people who worked to make JWST an incredible discovery machine. AA acknowledges support by the Swedish research council Vetenskapsrådet (2021-05559). PD acknowledges support from the NWO grant 016.VIDI.189.162 (“ODIN”) and warmly thanks the European Commission’s and University of Groningen’s CO-FUND Rosalind Franklin program. M.K. was supported by the ANID BASAL project FB210003. AZ and LJF acknowledge support by Grant No. 2020750 from the United States-Israel Binational Science Foundation (BSF) and Grant No. 2109066 from the United States National Science Foundation (NSF); by the Ministry of Science & Technology, Israel; and by the Israel Science Foundation Grant No. 864/23.

Facilities: JWST/NIRSpec

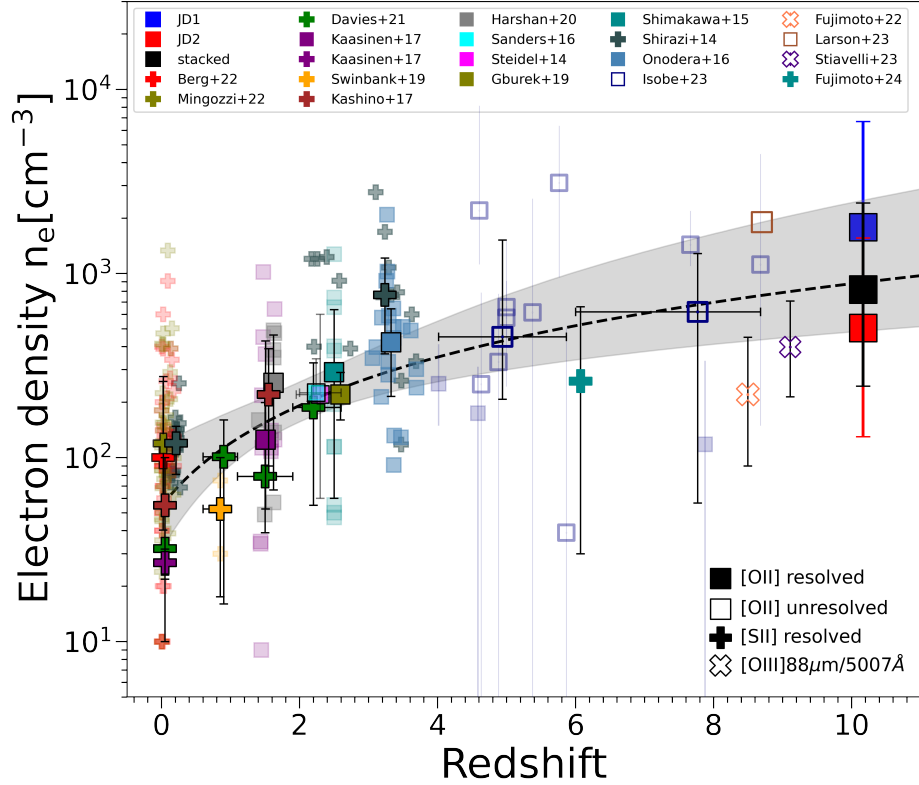


Figure 7. Electron densities of galaxies measured from $z = 0$ to 10. Our measurements for JD1, JD2, and the stacked spectrum are shown by the blue, red, and black squares, respectively. The rest of the n_e measurements are compiled from the literature. For local galaxies at $z \lesssim 0.2$: Berg et al. (2022), Davies et al. (2021), Kashino et al. (2017), Kaasinen et al. (2017), Shirazi et al. (2014), and Mingozzi et al. (2022). For $0.2 \lesssim z \lesssim 4$: Davies et al. (2021), Swinbank et al. (2019), Kashino et al. (2017), Kaasinen et al. (2017), Harshan et al. (2020), Sanders et al. (2016), Steidel et al. (2014), Shimakawa et al. (2015), Gburek et al. (2019), Onodera et al. (2016), and Shirazi et al. (2014). For $4 \lesssim z \lesssim 9$: Isobe et al. (2023), Larson et al. (2023), Fujimoto et al. (2022), Stiavelli et al. (2023), and Fujimoto et al. (2024). Different colors represent different studies, while different symbols represent various emission-line diagnostics used to derive n_e . Overall, there are three employed emission-line diagnostics to derive n_e : $R_{[\text{OII}]}$ (square), $R_{[\text{SII}]}$ (plus), and an indirect method using $[\text{OIII}] \lambda 88\mu\text{m}/\lambda 5007\text{\AA}$ ratio (cross). While $[\text{OII}] \lambda \lambda 3726, 3729$ doublet is resolved in the majority of the studies (indicated with closed squares), it is not resolved in some studies (indicated with open squares) because of the insufficient spectral resolution. For studies that reported n_e of the individual galaxies, we show those with transparent symbols, in addition to the median values shown with thick symbols. The black dashed line represents the best-fit power-law function in the form of $n_e = A \times (1+z)^p$ with $A = 54_{-22}^{+31} \text{ cm}^{-3}$ and $p = 1.2 \pm 0.4$. The gray shaded area shows 2σ uncertainty around the best-fit line.

Software: GRIZLI (Brammer et al. 2022) astropy (The Astropy Collaboration et al. 2018), matplotlib (Hunter 2007), NumPy (Harris et al. 2020), SciPy (Virtanen et al. 2020), STScI JWST Calibration Pipeline

(jwst-pipeline.readthedocs.io (Rigby et al. 2023) IDL Astronomy Library: idlastro.gsfc.nasa.gov (Landsman 1993), PIXEDFIT (Abdurro’uf et al. 2021, 2022), MSAEXP, PYNEB (Luridiana et al. 2015)

APPENDIX

A. GENERAL FORMULA FOR THE RELATIONSHIP BETWEEN $R_{[\text{OII}]}$ AND n_e

We perform interpolation to the model grids of Kewley et al. (2019a) to construct a general functional formula for calculating n_e from $R_{[\text{OII}]}$ given an electron temperature (T_e). The model grids of Kewley et al. (2019a) give the

Table 4. Coefficients for the polynomial function in Eq. A2

Coefficient	a	b	c	d
α	-0.00447	0.28813	-0.06841	0.00506
β	-7616.41042	7075.85077	-2433.11054	321.56781
γ	-1661.48935	1481.10495	-507.35920	69.67036

relationship between n_e and $R_{[\text{O II}]}$ for three different electron temperatures ($\log(T_e/\text{K}) = 3.5, 4.0,$ and 4.5). The model grids were generated using the MAPPINGS version 5.1 photoionization code (Binette et al. 1985; Sutherland & Dopita 1993; Dopita et al. 2015). To get a functional formula out of the curves, we fit each $R_{[\text{O II}]}(n_e)$ curve with the following functional form adapted from Sanders et al. (2016):

$$n_e = \frac{\gamma R_{[\text{O II}]} - \alpha \beta}{\alpha - R_{[\text{O II}]}}. \quad (\text{A1})$$

We then interpolate the $R_{[\text{O II}]}(n_e)$ curves using the cubic spline method for 9 values of $\log(T_e)$ between 3.5 and 4.5. For each interpolated curve, we perform fitting with Eq. A1 to get the coefficients (α , β , and γ) and investigate their dependencies with T_e . We show the relations between those coefficients and T_e in Figure 8. The blue crosses represent the coefficients of the original curves from Kewley et al. (2019a), while the gray circles are from the interpolated curves. The relations can be well-fitted with a cubic polynomial function of the form

$$\alpha, \beta, \gamma = a + bx + cx^2 + dx^3 \quad (\text{A2})$$

with $x = \log(T_e)$. The best-fit cubic polynomial functions are shown as red dashed lines in Figure 8 and their coefficients are summarized in Table 4. We show models $R_{[\text{O II}]}(n_e)$ for 9 values of T_e in Figure 5.

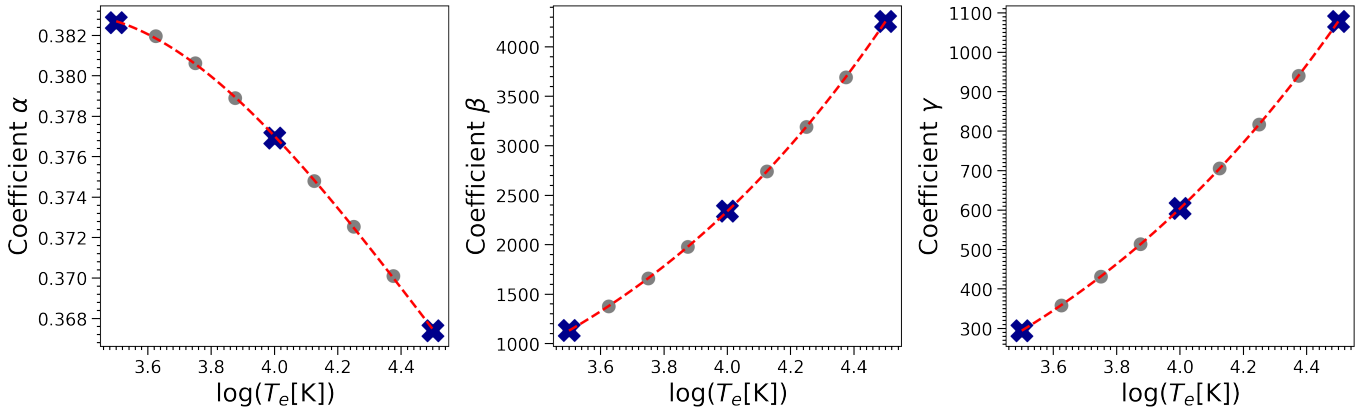


Figure 8. The dependence of the coefficients in Equation A1 to the electron temperature (T_e ; in logarithmic scale). The blue crosses represent the coefficients of the original $R_{[\text{O II}]}(n_e)$ curves from Kewley et al. (2019a) at $\log(T_e/\text{K}) = 3.5, 4.0,$ and 4.5 . The gray circles show the coefficients of the interpolated curves at 9 values of T_e . The red dashed lines show the best-fit cubic polynomial functions.

B. CORNER PLOTS OF THE FITTING ON $[\text{O II}] \lambda\lambda 3726, 3729$ DOUBLET

Figure 9 shows the corner plots showing the posterior probability distributions from the MCMC fitting of the $[\text{O II}] \lambda\lambda 3726, 3729$ doublet of JD1 (top left), JD2 (top right), and the stacked spectrum (bottom). Only some parameters are shown in the corner plots, including the individual line fluxes of $[\text{O II}] \lambda\lambda 3726, 3729$ doublet, FWHM, and electron density. Among those parameters, only FWHM is a free parameter, while the others are dependent parameters. Other free parameters, including the peak wavelength and amplitude, are not shown in the corner plots.

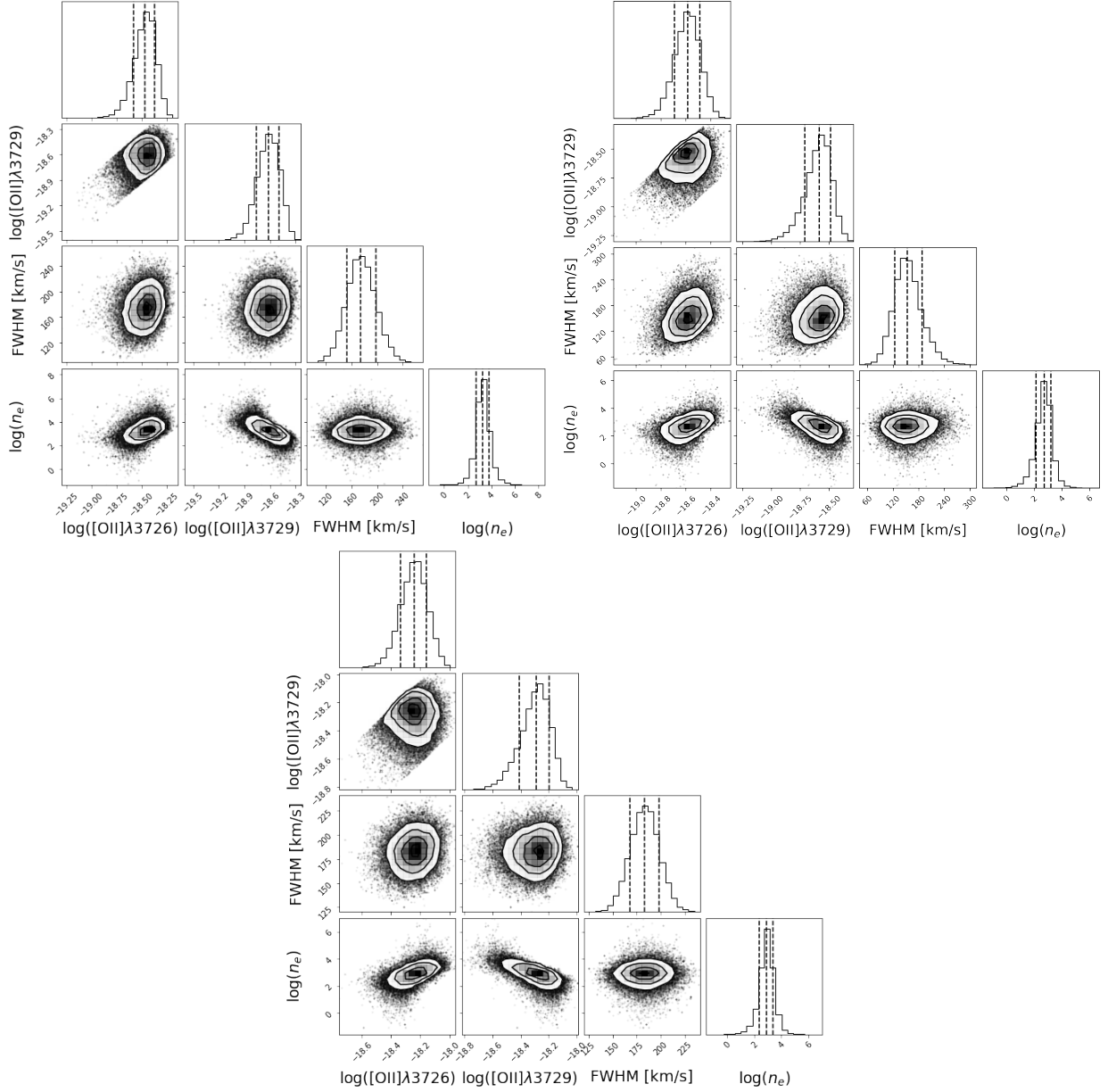


Figure 9. Corner plots showing the posterior probability distributions of some parameters in the MCMC fitting of the $[\text{O II}]\lambda\lambda 3726, 3729$ doublet. The top left, top right, and bottom panels show the corner plots for JD1, JD2, and stacked spectrum, respectively. Other free parameters, including the central wavelength and amplitude, are not shown here. The fluxes of $[\text{O II}]\lambda 3726$ and $[\text{O II}]\lambda 3729$ are dependent parameters.

C. MEASURED EMISSION LINES FROM THE NIRSPEC PRISM SPECTRA

The NIRSPEC prism spectra of JD1 and JD2 were obtained by JWST program GO 1433 (PI Coe) and presented in Hsiao et al. (2023a). There were two separate NIRSPEC multi-object spectroscopy (MOS) observations (Obs 21 and Obs 23) using the low-resolution ($R \sim 30 - 300$) prism spanning a wavelength coverage of $0.6 - 5.3 \mu\text{m}$. Obs 23 was performed with standard 3-slitlet nods, while Obs 21 was performed with single slitlets. Each observation had a total exposure time of 1.8 hours (3.6 hours). In Hsiao et al. (2023a), the emission lines were measured from the stacked spectrum of the four spectra (JD1 Obs 21, JD1 Obs 23, JD2 Obs 21, and JD2 Obs 23). Here, we revisit the analysis and measure the emission lines in the individual spectra. Moreover, we use the latest reduced spectra from The Dawn

Table 5. Measured Emission Line Properties from NIRSpec prism spectra

Emission Line	λ rest	JD1 Obs 21 Flux	JD1 Obs 23 Flux	JD2 Obs 21 Flux	JD2 Obs 23 Flux	Stacked Flux
(1)	(2)	(3)	(4)	(5)	(6)	(7)
[C III]	1906.68,1908.73	95^{+15}_{-14}	98^{+21}_{-21}	194^{+17}_{-17}	129^{+21}_{-20}	428^{+34}_{-35}
[O II]	3727.10,3729.86	17^{+5}_{-4}	34^{+7}_{-7}	50^{+5}_{-5}	30^{+5}_{-5}	144^{+12}_{-12}
[Ne III]	3869.86	19^{+6}_{-5}	35^{+6}_{-5}	54^{+5}_{-5}	51^{+8}_{-7}	177^{+12}_{-12}
[Ne III]	3968.59	...	14^{+8}_{-6}	33^{+5}_{-4}	20^{+5}_{-5}	88^{+10}_{-10}
H δ	4102.89	15^{+5}_{-5}	34^{+7}_{-7}	27^{+5}_{-4}	19^{+5}_{-5}	117^{+55}_{-17}
H γ	4341.69	21^{+4}_{-4}	58^{+9}_{-8}	65^{+6}_{-6}	34^{+6}_{-6}	179^{+13}_{-12}
[O III]	4364.44	...	12^{+3}_{-3}	13^{+3}_{-3}	28^{+7}_{-7}	62^{+5}_{-5}
He I	4472.735	26^{+9}_{-8}	12^{+6}_{-6}	36^{+13}_{-12}

NOTE—(1) Emission line. (2) Rest-frame wavelength. (3) Measured line fluxes of the JD1 Obs 21 spectrum. (4) Measured line fluxes of the JD1 Obs 23 spectrum. (5) Measured line fluxes of the JD2 Obs 21 spectrum. (6) Measured line fluxes of the JD2 Obs 23 spectrum. (7) Measured line fluxes from the stacked sum of the four spectra (JD1 Obs21 + JD1 Obs23 + JD2 Obs21 + JD2 Obs23). All flux densities are in units of 10^{-20} erg s $^{-1}$ cm $^{-2}$ Å $^{-1}$. The line fluxes are not corrected for the lensing magnifications (8.0 and 5.3 for JD1 and JD2, respectively) and slit loss.

JWST Archive (DJA)⁴, which were reduced using the upgraded MSAEXP⁵ version 0.6.7. The NIRSpec data reduction is described in Heintz et al. (2023b) and Heintz et al. (2024). We fit the NIRSpec prism spectra and measure the emission line fluxes using PIXEDFIT. Besides the individual spectra, we also fit the stacked sum of the four spectra (i.e., JD1 Obs 21 + JD1 Obs 23 + JD2 Obs 21 + JD2 Obs 23).

The fitting results for the individual spectra are shown in Figure 10 alongside the slitlets configurations overlaid on $1.6'' \times 1.6''$ NIRCcam color images. We show the fitting result of the stacked spectrum in Figure 11. We note that most of the observations target the brighter component A. Only Obs 21 on JD2 covers both components A and B. We also note that slitlets do not cover the same area in the two observations, causing the differences in emission line fluxes. The black line and gray shaded area represent the observed spectra and their 1σ uncertainties. The blue and red lines represent the best-fit continuum and Gaussian models of the detected emission lines. The spectra roll off gradually from $\sim 1.5 \mu\text{m}$ (1343 Å rest-frame) to the Lyman break observed at $1.36 \mu\text{m}$ (1216 Å), instead of a sharp break. This is due to the Lyman- α damping wing (see Hsiao et al. 2023a; Heintz et al. 2023b). The continuum modeled here does not include the modeling of Lyman- α damping wing which makes the discrepancy between the models and observed spectra around the wavelength range. The best-fit continuum is obtained from SED fitting on the spectrum after masking the emission lines and cutting at $1.5 < \lambda < 5.2 \mu\text{m}$.

Table 5 summarizes the measured emission line properties. The line fluxes are not corrected for the lensing magnifications (8.0 and 5.3 for JD1 and JD2, respectively) and slit loss. The slit loss corrections can be estimated by taking the ratio between the total aperture photometry in NIRCcam filters, obtained from the GRIZLI pipeline (Brammer et al. 2022) (see Hsiao et al. 2023a), and pseudo photometry obtained by integrating the NIRSpec spectra through the NIRCcam filters. Then the correction factors at the emission lines can be estimated by interpolating the wavelength-dependent flux ratio. The correction factors for the listed lines in Table 5 are the following. JD1 Obs 21 = [2.5, 3.7, 3.9, 4.0, 4.2, 4.6, 4.6, 4.6], JD1 Obs 23 = [2.2, 3.3, 3.4, 3.5, 3.7, 4.0, 4.0, 4.0], JD2 Obs 21 = [2.7, 2.4, 2.4, 2.4, 2.3, 2.0, 2.0, 2.0], and JD2 Obs 23 = [2.0, 2.5, 2.6, 2.6, 2.7, 2.8, 2.8, 2.8].

REFERENCES

⁴ <https://dawn-cph.github.io/dja/>

⁵ <https://github.com/gbrammer/msaexp>

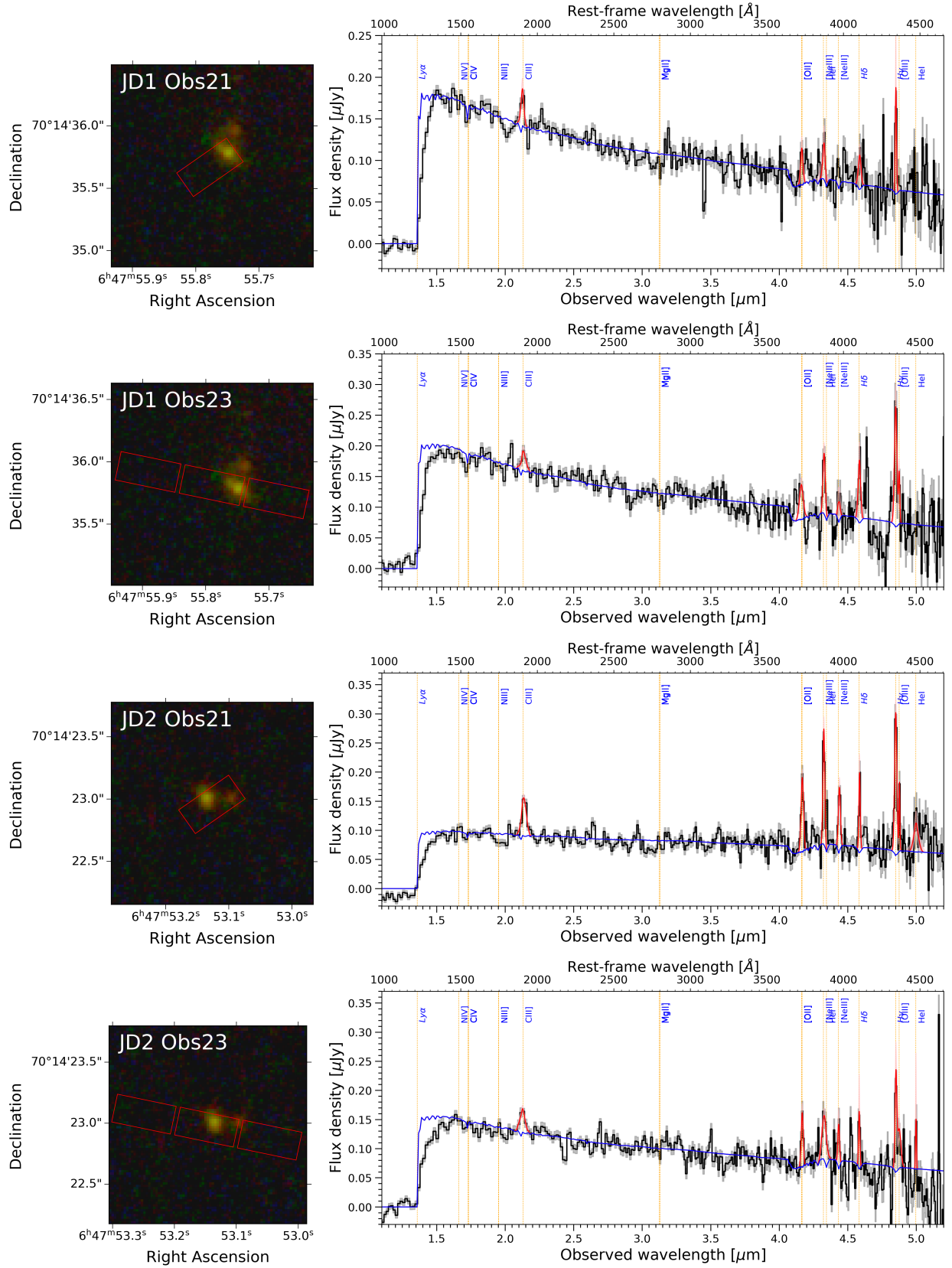


Figure 10. NIRSpect prism spectra of JD1 and JD2 from two separate observations (Obs 21 and Obs 23). The observations were performed by the JWST program GO 1433 (PI Coe) and the original data were presented in [Hsiao et al. \(2023a\)](#). *Left:* Slitlet configurations overlaid on $1.6'' \times 1.6''$ NIRCcam color images. Note that most of the observations target the brighter component A. Only JD2 Obs 21 covers both components A and B. *Right:* NIRSpect prism spectra (black line and gray shaded area) and the best-fit model continuum (blue) and Gaussian for the emission lines (red). The SED modeling does not include the Lyman- α damping wing which makes the discrepancy between the best-fit continuum and the observed spectrum around the Lyman- α wavelength.

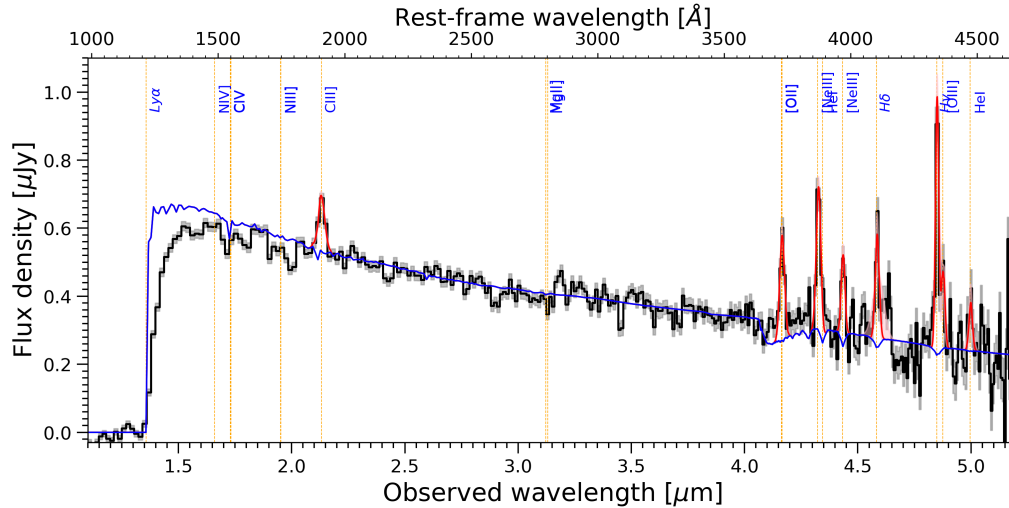


Figure 11. The stacked sum of the four spectra shown in Figure 10 (i.e., JD1 Obs 21 + JD1 Obs 23 + JD2 Obs 21 + JD2 Obs 23) and its fitting result. The line and symbols are the same as those in Figure 10.

Abazajian, K. N., Adelman-McCarthy, J. K., Agüeros, M. A., et al. 2009, *ApJS*, 182, 543, doi: [10.1088/0067-0049/182/2/543](https://doi.org/10.1088/0067-0049/182/2/543)

Abdurro'uf, Lin, Y.-T., Wu, P.-F., & Akiyama, M. 2021, *ApJS*, 254, 15, doi: [10.3847/1538-4365/abebe2](https://doi.org/10.3847/1538-4365/abebe2)

—. 2022, piXedfit: Analyze spatially resolved SEDs of galaxies, *Astrophysics Source Code Library*, record ascl:2207.033

Abdurro'uf, Coe, D., Jung, I., et al. 2023, *ApJ*, 945, 117, doi: [10.3847/1538-4357/acba06](https://doi.org/10.3847/1538-4357/acba06)

Backhaus, B. E., Trump, J. R., Pirzkal, N., et al. 2024, *ApJ*, 962, 195, doi: [10.3847/1538-4357/ad1520](https://doi.org/10.3847/1538-4357/ad1520)

Bacon, R., Conseil, S., Mary, D., et al. 2017, *A&A*, 608, A1, doi: [10.1051/0004-6361/201730833](https://doi.org/10.1051/0004-6361/201730833)

Berg, D. A., James, B. L., King, T., et al. 2022, *ApJS*, 261, 31, doi: [10.3847/1538-4365/ac6c03](https://doi.org/10.3847/1538-4365/ac6c03)

Binette, L., Dopita, M. A., & Tuohy, I. R. 1985, *ApJ*, 297, 476, doi: [10.1086/163544](https://doi.org/10.1086/163544)

Böker, T., Beck, T. L., Birkmann, S. M., et al. 2023, *PASP*, 135, 038001, doi: [10.1088/1538-3873/acb846](https://doi.org/10.1088/1538-3873/acb846)

Brammer, G., Strait, V., Matharu, J., & Momcheva, I. 2022, *grizli*, 1.5.0, Zenodo, doi: [10.5281/zenodo.6672538](https://doi.org/10.5281/zenodo.6672538)

Brinchmann, J., Charlot, S., White, S. D. M., et al. 2004, *MNRAS*, 351, 1151, doi: [10.1111/j.1365-2966.2004.07881.x](https://doi.org/10.1111/j.1365-2966.2004.07881.x)

Bunker, A. J., Saxena, A., Cameron, A. J., et al. 2023, *A&A*, 677, A88, doi: [10.1051/0004-6361/202346159](https://doi.org/10.1051/0004-6361/202346159)

Cameron, A. J., Saxena, A., Bunker, A. J., et al. 2023, *A&A*, 677, A115, doi: [10.1051/0004-6361/202346107](https://doi.org/10.1051/0004-6361/202346107)

Castellano, M., Napolitano, L., Fontana, A., et al. 2024, *arXiv e-prints*, arXiv:2403.10238, doi: [10.48550/arXiv.2403.10238](https://doi.org/10.48550/arXiv.2403.10238)

Christensen, L., Jakobsen, P., Willott, C., et al. 2023, *A&A*, 680, A82, doi: [10.1051/0004-6361/202347943](https://doi.org/10.1051/0004-6361/202347943)

Coe, D., Zitrin, A., Carrasco, M., et al. 2013, *ApJ*, 762, 32, doi: [10.1088/0004-637X/762/1/32](https://doi.org/10.1088/0004-637X/762/1/32)

Croom, S. M., Lawrence, J. S., Bland-Hawthorn, J., et al. 2012, *MNRAS*, 421, 872, doi: [10.1111/j.1365-2966.2011.20365.x](https://doi.org/10.1111/j.1365-2966.2011.20365.x)

Curti, M., D'Eugenio, F., Carniani, S., et al. 2023, *MNRAS*, 518, 425, doi: [10.1093/mnras/stac2737](https://doi.org/10.1093/mnras/stac2737)

Davies, R. L., Förster Schreiber, N. M., Genzel, R., et al. 2021, *ApJ*, 909, 78, doi: [10.3847/1538-4357/abd551](https://doi.org/10.3847/1538-4357/abd551)

Davé, R., Finlator, K., & Oppenheimer, B. D. 2011, *Monthly Notices of the Royal Astronomical Society*, 416, 1354, doi: [10.1111/j.1365-2966.2011.19132.x](https://doi.org/10.1111/j.1365-2966.2011.19132.x)

Dopita, M. A., Fischera, J., Sutherland, R. S., et al. 2006a, *ApJS*, 167, 177, doi: [10.1086/508261](https://doi.org/10.1086/508261)

—. 2006b, *ApJ*, 647, 244, doi: [10.1086/505418](https://doi.org/10.1086/505418)

Dopita, M. A., Ho, I. T., Dressel, L. L., et al. 2015, *ApJ*, 801, 42, doi: [10.1088/0004-637X/801/1/42](https://doi.org/10.1088/0004-637X/801/1/42)

Ferruit, P., Jakobsen, P., Giardino, G., et al. 2022, *A&A*, 661, A81, doi: [10.1051/0004-6361/202142673](https://doi.org/10.1051/0004-6361/202142673)

Finkelstein, S. L., Bagley, M. B., Ferguson, H. C., et al. 2023, *ApJL*, 946, L13, doi: [10.3847/2041-8213/acade4](https://doi.org/10.3847/2041-8213/acade4)

Foreman-Mackey, D., Hogg, D. W., Lang, D., & Goodman, J. 2013, *PASP*, 125, 306, doi: [10.1086/670067](https://doi.org/10.1086/670067)

Fujimoto, S., Ouchi, M., Nakajima, K., et al. 2022, *arXiv e-prints*, arXiv:2212.06863, doi: [10.48550/arXiv.2212.06863](https://doi.org/10.48550/arXiv.2212.06863)

Fujimoto, S., Arrabal Haro, P., Dickinson, M., et al. 2023, *ApJL*, 949, L25, doi: [10.3847/2041-8213/acd2d9](https://doi.org/10.3847/2041-8213/acd2d9)

- Fujimoto, S., Ouchi, M., Kohno, K., et al. 2024, arXiv e-prints, arXiv:2402.18543, doi: [10.48550/arXiv.2402.18543](https://doi.org/10.48550/arXiv.2402.18543)
- Garcia, F. A. B., Ricotti, M., Sugimura, K., & Park, J. 2023, MNRAS, 522, 2495, doi: [10.1093/mnras/stad1092](https://doi.org/10.1093/mnras/stad1092)
- Gardner, J. P., Mather, J. C., Abbott, R., et al. 2023, PASP, 135, 068001, doi: [10.1088/1538-3873/acd1b5](https://doi.org/10.1088/1538-3873/acd1b5)
- Gburek, T., Siana, B., Alavi, A., et al. 2019, ApJ, 887, 168, doi: [10.3847/1538-4357/ab5713](https://doi.org/10.3847/1538-4357/ab5713)
- Hainline, K. N., D'Eugenio, F., Jakobsen, P., et al. 2024, arXiv e-prints, arXiv:2404.04325, doi: [10.48550/arXiv.2404.04325](https://doi.org/10.48550/arXiv.2404.04325)
- Harris, C. R., Millman, K. J., van der Walt, S. J., et al. 2020, Nature, 585, 357, doi: [10.1038/s41586-020-2649-2](https://doi.org/10.1038/s41586-020-2649-2)
- Harshan, A., Gupta, A., Tran, K.-V., et al. 2020, ApJ, 892, 77, doi: [10.3847/1538-4357/ab76cf](https://doi.org/10.3847/1538-4357/ab76cf)
- Heintz, K. E., Brammer, G. B., Giménez-Arteaga, C., et al. 2023a, Nature Astronomy, 7, 1517, doi: [10.1038/s41550-023-02078-7](https://doi.org/10.1038/s41550-023-02078-7)
- Heintz, K. E., Watson, D., Brammer, G., et al. 2023b, arXiv e-prints, arXiv:2306.00647, doi: [10.48550/arXiv.2306.00647](https://doi.org/10.48550/arXiv.2306.00647)
- Heintz, K. E., Brammer, G. B., Watson, D., et al. 2024, arXiv e-prints, arXiv:2404.02211, doi: [10.48550/arXiv.2404.02211](https://doi.org/10.48550/arXiv.2404.02211)
- Horne, K. 1986, PASP, 98, 609, doi: [10.1086/131801](https://doi.org/10.1086/131801)
- Hsiao, T. Y.-Y., Abdurro'uf, Coe, D., et al. 2023a, arXiv e-prints, arXiv:2305.03042, doi: [10.48550/arXiv.2305.03042](https://doi.org/10.48550/arXiv.2305.03042)
- Hsiao, T. Y.-Y., Coe, D., Abdurro'uf, et al. 2023b, ApJL, 949, L34, doi: [10.3847/2041-8213/acc94b](https://doi.org/10.3847/2041-8213/acc94b)
- Hunter, J. D. 2007, Computing in Science & Engineering, 9, 90, doi: [10.1109/MCSE.2007.55](https://doi.org/10.1109/MCSE.2007.55)
- Isobe, Y., Ouchi, M., Nakajima, K., et al. 2023, ApJ, 956, 139, doi: [10.3847/1538-4357/acf376](https://doi.org/10.3847/1538-4357/acf376)
- Jakobsen, P., Ferruit, P., Alves de Oliveira, C., et al. 2022, A&A, 661, A80, doi: [10.1051/0004-6361/202142663](https://doi.org/10.1051/0004-6361/202142663)
- James, B. L., Berg, D. A., King, T., et al. 2022, ApJS, 262, 37, doi: [10.3847/1538-4365/ac8008](https://doi.org/10.3847/1538-4365/ac8008)
- Jung, I., Finkelstein, S. L., Arrabal Haro, P., et al. 2023, arXiv e-prints, arXiv:2304.05385, doi: [10.48550/arXiv.2304.05385](https://doi.org/10.48550/arXiv.2304.05385)
- Kaasinen, M., Bian, F., Groves, B., Kewley, L. J., & Gupta, A. 2017, MNRAS, 465, 3220, doi: [10.1093/mnras/stw2827](https://doi.org/10.1093/mnras/stw2827)
- Kashino, D., Silverman, J. D., Sanders, D., et al. 2017, ApJ, 835, 88, doi: [10.3847/1538-4357/835/1/88](https://doi.org/10.3847/1538-4357/835/1/88)
- Kauffmann, G., Heckman, T. M., Tremonti, C., et al. 2003, MNRAS, 346, 1055, doi: [10.1111/j.1365-2966.2003.07154.x](https://doi.org/10.1111/j.1365-2966.2003.07154.x)
- Kewley, L. J., & Dopita, M. A. 2002, ApJS, 142, 35, doi: [10.1086/341326](https://doi.org/10.1086/341326)
- Kewley, L. J., Nicholls, D. C., Sutherland, R., et al. 2019a, ApJ, 880, 16, doi: [10.3847/1538-4357/ab16ed](https://doi.org/10.3847/1538-4357/ab16ed)
- Kewley, L. J., Nicholls, D. C., & Sutherland, R. S. 2019b, ARA&A, 57, 511, doi: [10.1146/annurev-astro-081817-051832](https://doi.org/10.1146/annurev-astro-081817-051832)
- Killi, M., Watson, D., Fujimoto, S., et al. 2023, MNRAS, 521, 2526, doi: [10.1093/mnras/stad687](https://doi.org/10.1093/mnras/stad687)
- Kriek, M., Shapley, A. E., Reddy, N. A., et al. 2015, ApJS, 218, 15, doi: [10.1088/0067-0049/218/2/15](https://doi.org/10.1088/0067-0049/218/2/15)
- Landsman, W. B. 1993, in Astronomical Society of the Pacific Conference Series, Vol. 52, Astronomical Data Analysis Software and Systems II, ed. R. J. Hanisch, R. J. V. Brissenden, & J. Barnes, 246
- Larson, R. L., Finkelstein, S. L., Kocevski, D. D., et al. 2023, ApJL, 953, L29, doi: [10.3847/2041-8213/ace619](https://doi.org/10.3847/2041-8213/ace619)
- Le Fèvre, O., Tasca, L. A. M., Cassata, P., et al. 2015, A&A, 576, A79, doi: [10.1051/0004-6361/201423829](https://doi.org/10.1051/0004-6361/201423829)
- Luridiana, V., Morisset, C., & Shaw, R. A. 2015, A&A, 573, A42, doi: [10.1051/0004-6361/201323152](https://doi.org/10.1051/0004-6361/201323152)
- Mingozzi, M., James, B. L., Arellano-Córdova, K. Z., et al. 2022, ApJ, 939, 110, doi: [10.3847/1538-4357/ac952c](https://doi.org/10.3847/1538-4357/ac952c)
- Mo, H. J., & White, S. D. M. 2002, MNRAS, 336, 112, doi: [10.1046/j.1365-8711.2002.05723.x](https://doi.org/10.1046/j.1365-8711.2002.05723.x)
- Nakajima, K., Ouchi, M., Isobe, Y., et al. 2023, ApJS, 269, 33, doi: [10.3847/1538-4365/acd556](https://doi.org/10.3847/1538-4365/acd556)
- Nanayakkara, T., Glazebrook, K., Kacprzak, G. G., et al. 2016, ApJ, 828, 21, doi: [10.3847/0004-637X/828/1/21](https://doi.org/10.3847/0004-637X/828/1/21)
- Oesch, P. A., Brammer, G., van Dokkum, P. G., et al. 2016, ApJ, 819, 129, doi: [10.3847/0004-637X/819/2/129](https://doi.org/10.3847/0004-637X/819/2/129)
- Ono, Y., Harikane, Y., Ouchi, M., et al. 2023, ApJ, 951, 72, doi: [10.3847/1538-4357/acd44a](https://doi.org/10.3847/1538-4357/acd44a)
- Onodera, M., Carollo, C. M., Lilly, S., et al. 2016, ApJ, 822, 42, doi: [10.3847/0004-637X/822/1/42](https://doi.org/10.3847/0004-637X/822/1/42)
- Ormerod, K., Conselice, C. J., Adams, N. J., et al. 2024, MNRAS, 527, 6110, doi: [10.1093/mnras/stad3597](https://doi.org/10.1093/mnras/stad3597)
- Osterbrock, D. E. 1989, Astrophysics of gaseous nebulae and active galactic nuclei
- Pentericci, L., McLure, R. J., Garilli, B., et al. 2018, A&A, 616, A174, doi: [10.1051/0004-6361/201833047](https://doi.org/10.1051/0004-6361/201833047)
- Reddy, N. A., Topping, M. W., Sanders, R. L., Shapley, A. E., & Brammer, G. 2023, ApJ, 952, 167, doi: [10.3847/1538-4357/acd754](https://doi.org/10.3847/1538-4357/acd754)
- Rigby, J., Perrin, M., McElwain, M., et al. 2023, PASP, 135, 048001, doi: [10.1088/1538-3873/acb293](https://doi.org/10.1088/1538-3873/acb293)
- Sanders, R. L., Shapley, A. E., Topping, M. W., Reddy, N. A., & Brammer, G. B. 2024, ApJ, 962, 24, doi: [10.3847/1538-4357/ad15fc](https://doi.org/10.3847/1538-4357/ad15fc)

- Sanders, R. L., Shapley, A. E., Kriek, M., et al. 2016, *ApJ*, 816, 23, doi: [10.3847/0004-637X/816/1/23](https://doi.org/10.3847/0004-637X/816/1/23)
- Shibuya, T., Ouchi, M., & Harikane, Y. 2015, *ApJS*, 219, 15, doi: [10.1088/0067-0049/219/2/15](https://doi.org/10.1088/0067-0049/219/2/15)
- Shimakawa, R., Kodama, T., Steidel, C. C., et al. 2015, *MNRAS*, 451, 1284, doi: [10.1093/mnras/stv915](https://doi.org/10.1093/mnras/stv915)
- Shirazi, M., Brinchmann, J., & Rahmati, A. 2014, *ApJ*, 787, 120, doi: [10.1088/0004-637X/787/2/120](https://doi.org/10.1088/0004-637X/787/2/120)
- Silverman, J. D., Kashino, D., Sanders, D., et al. 2015, *ApJS*, 220, 12, doi: [10.1088/0067-0049/220/1/12](https://doi.org/10.1088/0067-0049/220/1/12)
- Steidel, C. C., Rudie, G. C., Strom, A. L., et al. 2014, *ApJ*, 795, 165, doi: [10.1088/0004-637X/795/2/165](https://doi.org/10.1088/0004-637X/795/2/165)
- Stiavelli, M., Morishita, T., Chiaberge, M., et al. 2023, *ApJL*, 957, L18, doi: [10.3847/2041-8213/ad0159](https://doi.org/10.3847/2041-8213/ad0159)
- Stott, J. P., Swinbank, A. M., Johnson, H. L., et al. 2016, *MNRAS*, 457, 1888, doi: [10.1093/mnras/stw129](https://doi.org/10.1093/mnras/stw129)
- Sugimura, K., Ricotti, M., Park, J., Garcia, F. A. B., & Yajima, H. 2024, arXiv e-prints, arXiv:2403.04824, doi: [10.48550/arXiv.2403.04824](https://doi.org/10.48550/arXiv.2403.04824)
- Sutherland, R. S., & Dopita, M. A. 1993, *ApJS*, 88, 253, doi: [10.1086/191823](https://doi.org/10.1086/191823)
- Swinbank, A. M., Harrison, C. M., Tiley, A. L., et al. 2019, *MNRAS*, 487, 381, doi: [10.1093/mnras/stz1275](https://doi.org/10.1093/mnras/stz1275)
- Tacchella, S., Eisenstein, D. J., Hainline, K., et al. 2023, *ApJ*, 952, 74, doi: [10.3847/1538-4357/acdbc6](https://doi.org/10.3847/1538-4357/acdbc6)
- Tang, M., Stark, D. P., Chen, Z., et al. 2023, *MNRAS*, 526, 1657, doi: [10.1093/mnras/stad2763](https://doi.org/10.1093/mnras/stad2763)
- The Astropy Collaboration, Price-Whelan, A. M., Sipőcz, B. M., et al. 2018, *AJ*, 156, 123, doi: [10.3847/1538-3881/aabc4f](https://doi.org/10.3847/1538-3881/aabc4f)
- Treu, T., Roberts-Borsani, G., Bradac, M., et al. 2022, *ApJ*, 935, 110, doi: [10.3847/1538-4357/ac8158](https://doi.org/10.3847/1538-4357/ac8158)
- Urrutia, T., Wisotzki, L., Kerutt, J., et al. 2019, *A&A*, 624, A141, doi: [10.1051/0004-6361/201834656](https://doi.org/10.1051/0004-6361/201834656)
- Virtanen, P., Gommers, R., Oliphant, T. E., et al. 2020, *Nature Methods*, 17, 261, doi: [10.1038/s41592-019-0686-2](https://doi.org/10.1038/s41592-019-0686-2)
- Williams, H., Kelly, P. L., Chen, W., et al. 2023, *Science*, 380, 416, doi: [10.1126/science.adf5307](https://doi.org/10.1126/science.adf5307)
- Wisnioski, E., Förster Schreiber, N. M., Wuyts, S., et al. 2015, *ApJ*, 799, 209, doi: [10.1088/0004-637X/799/2/209](https://doi.org/10.1088/0004-637X/799/2/209)
- Yuan, T.-T., Kewley, L. J., & Richard, J. 2012, *The Astrophysical Journal*, 763, 9, doi: [10.1088/0004-637X/763/1/9](https://doi.org/10.1088/0004-637X/763/1/9)